Journal of Advances in Modeling Earth Systems

RESEARCH ARTICLE
10.1029/2017MS001242

This article is a companion to Crueger et al. (2018) https://doi.org/10.1029/2017MS001233.

Key Points:
- Physics package for climate modeling is coupled to a nonhydrostatic dynamical core
- Tuning in five steps to obtain a balanced net radiation at top of atmosphere
- Overall biases of ICON-A are comparable to ECHAM6.3, but circulation biases remain due to problems with parameterized drag

Correspondence to:
M. A. Giorgetta,
marco.giorgetta@mpimet.mpg.de

Citation:
Giorgetta, M. A., Brokopf, R., Crueger, T., Esch, M., Fiedler, S., Helmert, J., et al. (2018). ICON-A, the atmosphere component of the ICON Earth system model: I. Model description. *Journal of Advances in Modeling Earth Systems*, *10*, 1613–1637. https://doi.org/10.1029/2017MS001242

Received 15 NOV 2017
Accepted 7 MAY 2018
Accepted article online 8 JUN 2018
Published online 21 JUL 2018

ICON-A, the Atmosphere Component of the ICON Earth System Model: I. Model Description

M. A. Giorgetta[1], R. Brokopf[1], T. Crueger[1], M. Esch[1], S. Fiedler[1], J. Helmert[2], C. Hohenegger[1], L. Kornblueh[1], M. Köhler[2], E. Manzini[1], T. Mauritsen[1], C. Nam[1,3], T. Raddatz[1], S. Rast[1], D. Reinert[2], M. Sakradzija[1], H. Schmidt[1], R. Schneck[1], R. Schnur[1], L. Silvers[4], H. Wan[5], G. Zängl[2], and B. Stevens[1]

[1]Max Planck Institute for Meteorology, Hamburg, Germany, [2]Deutscher Wetterdienst, Offenbach, Germany, [3]Institute for Meteorology, University of Leipzig, Leipzig, Germany, [4]Princeton University/GFDL, Princeton, NJ, USA, [5]Pacific Northwest National Laboratory, Richland, WA, USA

Abstract ICON-A is the new icosahedral nonhydrostatic (ICON) atmospheric general circulation model in a configuration using the Max Planck Institute physics package, which originates from the ECHAM6 general circulation model, and has been adapted to account for the changed dynamical core framework. The coupling scheme between dynamics and physics employs a sequential updating by dynamics and physics, and a fixed sequence of the physical processes similar to ECHAM6. To allow a meaningful initial comparison between ICON-A and the established ECHAM6-LR model, a setup with similar, low resolution in terms of number of grid points and levels is chosen. The ICON-A model is tuned on the base of the Atmospheric Model Intercomparison Project (AMIP) experiment aiming primarily at a well balanced top-of atmosphere energy budget to make the model suitable for coupled climate and Earth system modeling. The tuning addresses first the moisture and cloud distribution to achieve the top-of-atmosphere energy balance, followed by the tuning of the parameterized dynamic drag aiming at reduced wind errors in the troposphere. The resulting version of ICON-A has overall biases, which are comparable to those of ECHAM6. Problematic specific biases remain in the vertical distribution of clouds and in the stratospheric circulation, where the winter vortices are too weak. Biases in precipitable water and tropospheric temperature are, however, reduced compared to the ECHAM6. ICON-A will serve as the basis of further development and as the atmosphere component to the coupled model, ICON-Earth system model (ESM).

Plain Language Summary ICON-A is a new atmospheric model as needed for research on the general circulation of the atmosphere, or as atmospheric component in an Earth system model, as used in climate research. This article describes the construction of the atmospheric model, in particular how two major parts are coupled to each other: "dynamics" and "physics." Dynamics is the part that solves the equations for the atmospheric motion, temperature, density, and concentrations of water vapor, cloud water, and cloud ice. Physics is the part that computes the changes in these fields related to processes like radiation, cloud condensation, or turbulence. These physical changes depend on the state of the atmosphere as computed by the dynamics, and the changes computed by physics force change in the dynamics. The article documents the details of this construction. Further, the article describes how the physics is tuned to obtain a good representation of the general circulation of the period 1979 to 1988 in comparison to observations. A more detailed evaluation of such simulations is presented in a companion article by Crueger et al. (2018, https://doi.org/10.1029/2017MS001233).

1. Introduction

The ICON atmosphere general circulation model ICON-A is developed within the ICON modeling system for global atmosphere-only or coupled Earth system simulations. Through this development the advantages of the ICON modeling system shall be exploited in climate simulations, including (i) the option for very high resolution, based on the nonhydrostatic dynamics; (ii) the tracer mass conservation of the transport scheme; and (iii) the scalability allowing to exploit large computing systems. As a first step the ICON-A model is developed in a setup that makes it comparable to the established ECHAM6 atmosphere model in low-resolution (LR) configuration.

To this aim, the decision was taken to transfer the entire physics package of the ECHAM6 model to the ICON model, thus to aim at a model with similar forcing characteristics as known from the ECHAM6 model. This transfer requires the replacement of the dynamics-physics coupling interface to account for the differences between ECHAM and ICON in the equations (hydrostatic versus nonhydrostatic), the spatial discretization (spectral + Gauss grid versus icosahedral c-grid), the vertical coordinate system (pressure based versus height based), and the time stepping scheme (3 time level leapfrog versus 2 time level explicit). Further, differences in the model infrastructure, for instance, in the memory organization, had to be considered. The formulation of the physics was changed only in a few points, as described later.

Theoretically, it is clear that the transfer of the complete physics package from the ECHAM6 model, within which the physics has been developed, to the new ICON model is feasible. Practically, however, details of the implementations can be quite intricate and nontrivial to resolve. It is neither clear that the physics has been implemented entirely correctly in the old model, nor can we know whether the implementation in the new model is entirely correct. Therefore, this work aims at a comparison of both models on the basis of a meaningful experiment, the Atmospheric Model Intercomparison Project (AMIP) experiment (Gates, 1992; Taylor et al., 2000).

The preparation of the new ICON-A model also includes tuning of physical parameterizations, which is started from the original ECHAM6.3 setup. The tuning required a small number of changes only, so that we assume that the physics in ECHAM and ICON work in a very similar way, as originally intended. This development provides a base for future climate or Earth system simulations in the ICON Earth system model (ICON-ESM) at possibly much higher resolution.

The ICON-A model configuration differs from other configurations aiming at short and highly resolved global numerical weather prediction (Zängl et al., 2015), regional large eddy resolving simulations (Heinze et al., 2017), or highly idealized simulations (Dipankar et al., 2015; Silvers et al., 2016) in the parameterized forcing of the physical processes and in the coupling between the dynamics and the physics, which are documented in the following. The ICON-A model is developed on the basis of the AMIP experiment (Gates, 1992; Taylor et al., 2000) and tuned for a grid resolution of ~160 km and 47 layers resolving the atmosphere up to 80 km height. This configuration is chosen to allow a direct comparison to the similarly resolved ECHAM6-LR model (Stevens et al., 2013). The focus of this article is on the documentation of this configuration of ICON-A and the tuning process, while the companion article by Crueger et al. (2018) presents a quantitative evaluation of the climate mean state and variability of the ICON AMIP simulation, including a comparison to ECHAM6 AMIP simulations and to higher resolution setups.

In the following, the experimental details of the AMIP experiment are described in section 2. The dynamics physics coupling scheme is presented in section 3, followed by the description of the physics package in section 4. Section 5 describes the model tuning for the AMIP experiment, followed by the conclusions in section 6.

2. Setup of the AMIP Experiment

The AMIP experiment aims at reproducing the atmospheric climate of the past few decades, from 1979 to near present, for given transient ocean surface conditions, atmospheric composition, and solar irradiance. For the development and tuning of ICON-A, however, only the initial decade (1979 to 1988) is used. This suffices for the development process because of the generally short time scales of the atmospheric processes. The accompanying study by Crueger et al. (2018), however, evaluates the 30-year period 1979 to 2008, so that only one third of the years of their AMIP simulations is directly associated with the tuning process. The horizontal and vertical grids used for the model setup, the external data for the AMIP forcing, and the initial data are documented in the following.

2.1. Horizontal Grid

The horizontal grid is derived from a spherical icosahedron by repeated subdivision of the spherical triangular cells into smaller cells (Wan et al., 2013). The initial root refinement step divides each edge into n equal sections and results in n^2 spherical triangles in each icosahedral spherical triangle. These triangles are, however, no longer equilateral, because the new vertices are shared by six cells unlike the vertices of the icosahedron, which are shared by five triangles. For the following refinement steps only bisections of the edges are used,

Table 1
ICON Grids of the Spherical Icosahedron (R1B0) and the R2 Family and Their Characteristic Numbers of Cells n_c, Edges n_e, Vertices n_v, Rows Between North and South Pole n_r, Tropical Row Triangles n_{trt}, and Tropical Row Rhombi n_{trr}, and the Mean Cell Area a, and Grid Resolution Δx

R	B	n_c	n_e	n_v	n_r	n_{trt}	n_{trr}	a (km^2)	Δx (km)
1	0	20	30	12	3	10	5	25,505,057.01	5,050.25
2	0	80	120	42	6	20	10	6,376,264.25	2,525.13
2	1	320	480	162	12	40	20	1,594,066.06	1,262.56
2	2	1,280	1,920	642	24	80	40	398,516.52	631.28
2	3	5,120	7,680	2,562	48	160	80	99,629.13	315.64
2	4	20,480	30,720	10,242	96	320	160	24,907.28	157.82
2	5	81,920	122,880	40,962	192	640	320	6,226.82	78.91
2	6	327,680	491,520	163,842	384	1,280	640	1,556.71	39.46
2	7	1,310,720	1,966,080	655,362	768	2,560	1,280	389.18	19.73
2	8	5,242,880	7,864,320	2,621,442	1,536	5,120	2,560	97.29	9.86
2	9	20,971,520	31,457,280	10,485,762	3,072	10,240	5,120	24.32	4.93
2	10	83,886,080	125,829,120	41,943,042	6,144	20,480	10,240	6.08	2.47
2	11	335,544,320	503,316,480	167,772,162	12,288	40,960	20,480	1.52	1.23

resulting in four spherical triangles in each original cell. Combining the initial root (R) division in n sections with m bisection (B) steps thus results in a so-called *RnBm* grid with $n_c = 20 \cdot n^2 \cdot 4^m$ cells, $n_e = 3/2 \cdot n_c$ edges, and $n_v = n_c/2 + 2$ vertices. The mean area of the cells is $a = 4 \cdot \pi \cdot r^2/n_c$, where r is the radius of the sphere. The nominal mean resolution of an *RnBm* grid can then be defined as Δx = SQRT (a) = $r/n/2^m \cdot$ SQRT ($\pi/5$).

The icosahedron is oriented such that two opposite vertices of the icosahedron coincide with the North and South Pole and its northern five tropical vertices are located at longitudes 0°E + $k \cdot 72°$ longitude (k = 0 to 4) and 26.6°N, while the southern ones are located at longitudes 36°E + $k \cdot 72°$ and 26.6°S. In this configuration the triangles are arranged in $n_r = 3 \cdot n \cdot 2^m$ rows around the N-S axis with a constant number of $n_{trt} = 10 \cdot n \cdot 2^m$ triangular cells per row in the area of the $n_{tr} = n \cdot 2^m$ tropical rows covered by the tropical triangles of the north-south oriented spherical icosahedron. Polar rows have a linearly decreasing, odd number of cells per row with $n_{prt}(j_r) = 5 \cdot (2 \cdot j_r - 1)$ triangles in row j_r, counting from the adjacent North or South Pole. Note that the smallest periodic unit in the tropical rows consists of a rhombus formed by a pair of triangles. Tropical rows contain $n_{trr} = 5 \cdot n \cdot 2^m$ of such rhombi. For remapping data from an icosahedral *RnBm* grid to a regular latitude longitude grid, a grid of n_r latitudes and n_{trr} longitudes therefore is an economic natural choice, for instance, for computing zonal mean statistics, unless oversampling is needed.

The position of the vertices within the icosahedral triangles is optimized using the spring method of Tomita et al. (2001) with the spring coefficient $\beta = 0.9$ at each refinement step, which is helpful in making the triangular cells on average more uniform in shape.

Table 1 presents the characteristics for the spherical icosahedron and the derived *R2* grid family up to a resolution of 1.23 km, for an Earth radius $r = r_E$ = 6,371.229 km. In this work, however, only the R2B4 grid with 20,480 cells and a mean resolution of 158 km is used, which we consider the coarsest resolution that captures the baroclinic waves and related eddy fluxes with acceptable errors, as observed in simplified Held-Suarez experiments (Wan et al., 2013). In the companion article by Crueger et al. (2018), also, the R2B6 grid with a mean resolution of 40 km is used. The highest tabulated resolution should allow for deep convection resolving simulations, albeit at very high computational costs.

The numbers of cells and rows of the *R2B4* grid, and also its mean grid resolutions are similar to the numbers of spectral transform points and latitudes of the Gaussian grid used in ECHAM6-LR (Stevens et al., 2013), with 96 latitudes and 192 longitudes yielding 18,432 points.

2.2. Vertical Grid

The vertical grid of ICON is a terrain following hybrid sigma height grid following Leuenberger et al. (2010). This grid consists of n_h half levels, including the surface and the model top level, and $n_f = n_h - 1$ full levels defined in the middle between half levels. Using a column index j_c and downward running index j_k, the model levels have heights $z_h(j_c, j_k)$ and $z_f(j_c, j_k) = (z_h(j_c, j_k) + z_h(j_c, j_k + 1))/2$. The topographic adjustment of the model

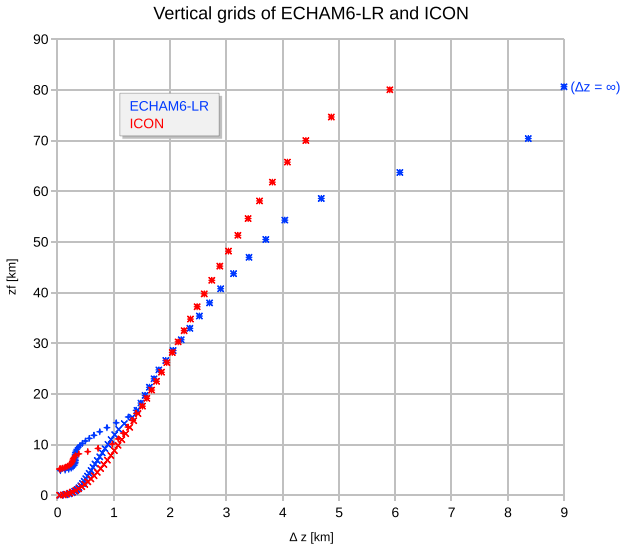

Figure 1. Full-level height *zf* (km) and layer thickness Δz (km) of the vertical grids of ICON and ECHAM6.3-LR. Both grids have 47 full levels with the topmost full level at 80 km. For each grid two profiles are shown, the first starting at sea level (cross symbols) and the second starting at a height of ~5 km (plus symbols). For ECHAM6.3-LR, which uses a hybrid sigma-pressure grid, half- and full-level heights z_h and z_f are computed from the original half and full level pressures $p_{h/f}$ as $z_{h/f} = H \cdot \ln(p_0/p_{h/f})$ with a scale height $H = 7$ km and $p_0 = 100{,}000$ Pa. The layer thickness is computed as the difference of the upper and lower half level height: $\Delta z = z_{h,\text{upper}} - z_{h,\text{lower}}$. In ECHAM6.3-LR, the pressure $p_{h,\text{top}}$ at the top of the model is 0 Pa yielding an infinite top layer thickness $\Delta z = \infty$.

level heights is limited to a maximum height $z_{h,\text{flat}}$. All higher levels up to the top height $z_{h,\text{top}}$ are pure height levels.

The actual grid used here for ICON-A (Figure 1, red) has 48 half levels up to $z_{h,1} = 83$ km, with the topmost full level at $z_{f,1} = 80$ km. The lowermost layer has a thickness of 40 m, independent of the surface height, and the transition height $z_{h,\text{flat}}$ to flat levels is set to 16 km. Between the surface and 16 km height, however, the levels vary in height depending on the height and spatial variability of the orography (cf. Leuenberger et al., 2010).

Over a flat surface at sea level, where $z_{h,48} = z_s = 0$, the 47 layers have thicknesses $\Delta z_f(j_c, j_k) = z_h(j_c, j_k) - z_h(j_c, j_k + 1)$ ranging from 40 m in the lowermost layer to ~0.3 km at 1 km height, ~1 km at 10 km, ~2 km at 30 km, ~3 km at 50 km, and ~6 km in the topmost layer. And the number of full levels up to 1, 16, and 50 km is 6, 23, and 39, respectively.

In comparison to the 47 level hybrid sigma pressure grid of ECHAM6-LR (Figure 1, blue), the ICON-A grid is slightly coarser in resolution in the upper troposphere than the ECHAM6-LR grid. Between ~16 and 32 km height the resolutions are very similar. Above 32 km, the ICON grid has a better resolution. Thus, this ICON grid has 16 levels in the stratosphere ($16 \text{ km} \leq z_f \leq 50$ km) and 8 levels in the mesosphere, while the ECHAM6-LR grid has 15 levels in the stratosphere and 6 in the mesosphere.

Due to their similarities it is expected that these 47 levels for ICON-A are as suitable for simulation of the general circulation as the 47-level grid used for ECHAM6-LR. Also, the limitations are expected to be similar, as, for instance, the insufficient vertical resolution of tropical waves will inhibit the simulation of the quasi-biennial oscillation in the equatorial stratosphere (Giorgetta et al., 2006; Krismer & Giorgetta, 2014).

2.3. Forcing Data of the AMIP Experiment

The transient forcing follows the recommendations for the CMIP6 version of the AMIP experiment (Eyring et al., 2016):

2.3.1. Sea Surface Temperature and Sea Ice Concentration

The monthly mean sea surface temperature and sea ice boundary conditions for the AMIP experiment were obtained from the input4MIPs project (https://esgf-node.llnl.gov/search/input4mips/, 2017–10-05). We use the preprocessed "boundary condition" data, which are meant to be used when daily fields are obtained from linear interpolation in time between given monthly mean values at the midpoints of the adjacent months. The preprocessing warrants that monthly means computed from the interpolated daily data reproduce the original monthly mean (Hurrell et al., 2008). The sea surface temperature and sea ice "boundary condition" data mostly differ from the observed monthly mean data in the vicinity of sea ice edges. It has been shown that in addition to preserving the observational monthly means, the seasonal cycle and interannual variance are more accurately represented.

2.3.2. Greenhouse Gases

Annual and global mean mole fractions of CO_2, CH_4, N_2O, CFC11, and CFC12 (Meinshausen et al., 2017) were obtained also from the input4MIPs project. Specifically, we use the version 1.2.0 data sets.

2.3.3. Ozone

Atmospheric ozone concentrations are prescribed as recommended by Hegglin et al. (Historical and future ozone database (1850–2100) in support of CMIP6, Geoscientific Model Development, in preparation). Also, this data set is available from the input4MIPs project. It provides ozone as monthly means in three spatial dimensions on an approximately 2° × 2.5° latitude-longitude grid with 66 vertical layers from 1,000 to 0.0001 hPa and is based on simulations performed within the framework of the Chemistry-Climate Model Initiative (CCMI) (Eyring et al., 2013) with the WACCM (Whole Atmosphere Community Climate Model) and CMAM (Canadian Middle Atmosphere Model) models. We have horizontally interpolated the ozone concentrations from the original latitude-longitude grid to the ICON grid using distance weighted interpolation.

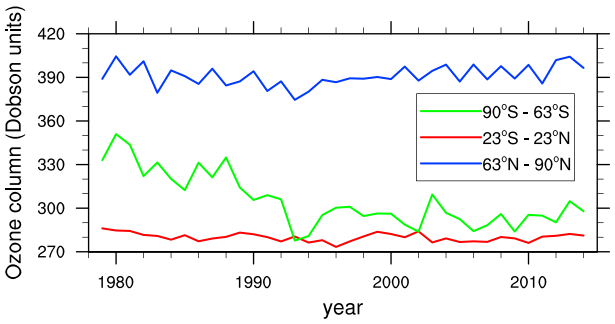

Figure 2. Annual mean total ozone column in Dobson units averaged over the polar caps (blue: 63°N–90°N, green: 63°S–90°S) and the tropics (red: 23°S–23°N), from 1979 to 2014.

Figure 2 shows the annual mean total ozone column averaged spatially for three selected latitude bands for the years 1979 to 2014. Obviously, the major interannual variation consists in the negative trend of the ozone column in the southern polar cap region due to the growth of the ozone hole until the early 1990s. Otherwise, the most prominent feature consists in the quasi-biennial variability of the annual mean ozone column exposed mostly in the polar regions.

2.3.4. Aerosol

ICON-A uses prescribed aerosol optical properties from natural and anthropogenic sources similar to ECHAM6.3. The aerosol optical depth (AOD), single-scattering albedo, and asymmetry parameter, used in the radiation transfer calculation, relate to stratospheric aerosol as well as natural and anthropogenic aerosol in the troposphere. The annual time series of global mean AOD from the three different sources, and for the spectral band ranging from 442 to 625 nm (approximately centered at 550 nm), is displayed in Figure 3 for giving an impression of the relative magnitudes of the AODs in ICON.

The natural aerosol in the stratosphere is of volcanic origin and characterized by strong year-to-year changes. Volcanic aerosol is prescribed with the data set from Stenchikov et al. (1998) that covers 1850 to 1999. Afterward the volcanic aerosol data of 1999 are repeated; that is, stratospheric AOD from 1999 onward is close to zero. Tropospheric natural aerosol consists primarily of mineral dust and sea spray with typical radii larger than 0.5 μm. These are prescribed as annually repeating monthly mean climatology from the Max Planck Institute aerosol climatology (MAC; Kinne et al., 2013) and read from external data files. Given the comparably large magnitude of natural AOD in the troposphere, we intend to refine the representation of the natural aerosol, particularly the variability of mineral dust, in the future.

Optical properties of natural aerosol are mixed with anthropogenic fine-mode aerosol in the troposphere. The anthropogenic aerosol optical properties are calculated with the simple plume parameterization MACv2-SP (Fiedler et al., 2017; Stevens et al., 2017). MACv2-SP parameterizes the optical properties of anthropogenic aerosol as a function of latitude, longitude, height, wavelength, and time. To do so, MACv2-SP represents the observed AOD by Gaussian functions in the horizontal and beta functions in the vertical direction. In total, MACv2-SP parameterizes anthropogenic aerosol plumes of five industrially polluted regions and four locations that are seasonally influenced by biomass burning. Characteristic annual cycles of each plume are represented through plume-wise monthly scalings adjusted to observed changes in AOD. For mimicking the historical evolution of the anthropogenic aerosol, MACv2-SP scales the AODs between 1850 and present-day using the anthropogenic aerosol emissions from CMIP6. In addition to the optical properties, MACv2-SP provides a scaling parameter for the cloud droplet number concentration that induces a Twomey effect in ICON's radiation calculation. The scaling is such that the strongest aerosol-cloud interaction occurs close to regional maxima in anthropogenic AOD.

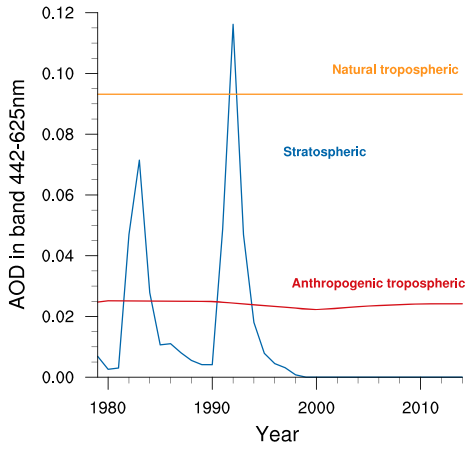

Figure 3. Time series of annual and global mean aerosol optical depth (AOD) between 442 and 625 nm from three sources: volcanic aerosol in the stratosphere (blue), tropospheric natural aerosols (orange), and tropospheric anthropogenic aerosols (red). The natural aerosol is annually repeating.

2.3.5. Spectral Solar Irradiance

Spectral solar irradiance (SSI) at the model top is prescribed as recommended by Matthes et al. (2017) for CMIP6 simulations. For the largest part of the spectrum, this data set has been calculated as an arithmetic mean of the SSI time series provided by the NRLSSI2 (Coddington et al., 2016) and SATIRE (Yeo et al., 2014) models. We use version 3.2 of the monthly mean data that is available at spectral resolution of 1 nm from the extreme UV to 750 nm and coarser resolution for longer wavelengths. We interpolate the data linearly in time and spectrally to the 14 solar bands of the PSrad scheme (cf. section 4.2). The small parts of the solar energy available at wavelengths shorter and longer than the range covered by the solar bands of PSrad (200 nm to 12.2 μm) have been added to the shortest and longest band of PSrad, respectively. Illustrations of the time series of total solar irradiation and SSI are given in Figures 1 and 2 of Matthes et al. (2017).

2.4. Initialization

Initial data for the prognostic atmospheric variables have been derived from European Centre for Medium-Range Weather Forecasts (ECMWF) analysis data. The original data are provided at the spectral truncation T1279 with 137 levels. These data are remapped to the according ICON resolutions. The selection of the data is consistent with the requirement of the German Weather Service for cold starting an ICON forecast cycle, if necessary, and uses the same set of rules and tools in adapting IFS data to ICON. As the operational archive at ECMWF does not provide high-resolution analysis data for the years 1978 and 1979, 2015 and 2016 have been selected and relabeled to 1978 and 1979, respectively. Considering the decadal duration of the AMIP experiments, and the climatological evaluation, this relabeling of years is acceptable.

3. Dynamics-Physics Coupling

The integration over time of the model equations is executed in the dynamical core, for which Zängl et al. (2015) provide the details. For the time stepping two time steps are distinguished within the dynamical core in order to allow time splitting between the fast dynamics involving acoustic waves, and slower processes. While fast dynamics is integrated with a short dynamics time step Δt_{dyn}, employing a predictor-corrector method, diffusion, tracer advection, and the physical forcing increments is computed at time steps $\Delta t = n \cdot \Delta t_{\mathrm{dyn}}$. Some physical processes may be computed even less frequently, at multiples of Δt. This time splitting allows for a computationally efficient integration in the presence of acoustic waves. Details of the splitting are given in the section 3.2.

In the setup used here, with a mean horizontal resolution of 158 km and a vertical range up the lower mesosphere, we use Δt_{dyn}. = 120 s and $\Delta t = 5 \cdot \Delta t_{\mathrm{dyn}} = 600$ s. The time step of 600 s is chosen here to be the same as in ECHAM6 in the LR setup (Stevens et al., 2013). For ECHAM6-LR, Δt = 600 s is practically the longest stable time step, with only exceptional numerical instabilities. For ICON-A, a longer maximum time step would be possible (see section 2.4 of Zängl et al., 2015).

3.1. Variable Transformations

The prognostic variables of the ICON model are normal wind v_n, vertical wind w, density ρ, virtual potential temperature θ_v, and tracer mass mixing ratios q_i with respect to the total air mass, as originally suggested by Gassmann and Herzog (2008). The normal wind v_n is the horizontal wind component on full levels that is perpendicular to the edge. The vertical wind w is defined on half level cell centers and all other variables on full level cell centers (Figure 4, left). For the prognostic variables, levels refer to height levels, see section 2.2.

The physical parameterizations are, however, formulated in a different set of variables: zonal wind u, meridional wind v, air mass per unit area m, temperature T, and tracer mass mixing ratios q_i, all defined on full-level cell centers (Figure 4, right), where levels refer to pressure levels. The half-level pressure p_h for the physics is diagnosed by integration of the hydrostatic equation, and the full-level pressure as $p_f = (p_{h,\mathrm{lower}} \cdot p_{h,\mathrm{upper}})^{0.5}$. The choice to provide a hydrostatic pressure to the physics is motivated by the fact that often parameterizations originating from hydrostatic models determine mass in layers from vertical pressure differences.

In the following X represents the set of prognostic variables (v_n, w, ρ, θ_v, and q_i) of the dynamics, while Y represents the set of variables used to compute the forcing (u, v, T, m, and q_i). The transformation $Y = \mathrm{Tr}_{\mathrm{d2p}}(X)$ is applied before computing the physical forcing, followed by a back transformation $(\partial X/\partial t)_{\mathrm{phy}} = \mathrm{Tr}_{\mathrm{p2d}}((\partial Y/\partial t)_{\mathrm{phy}})$. Note that these transformations, which include mapping operations between different points on the grid, are not exactly reversible, that is, $\mathrm{Tr}_{\mathrm{p2d}} \circ \mathrm{Tr}_{\mathrm{d2p}} \neq 1$. As pointed out in Zängl et al. (2015), applying transformed parameterized tendencies $(\partial X/\partial t)_{\mathrm{phy}}$ is numerically superior to applying parameterized tendencies $(\partial Y/\partial t)_{\mathrm{phy}}$ to transformed prognostic variables Y followed by their back transformation to the prognostic variables, owing to numerical "noise" resulting from the remapping between different points on the model grid.

3.2. Operator Splitting

The time integration scheme of the model generally propagates the prognostic state $X(t)$ forward in time in discrete time intervals Δt. This can be formalized by a model operator M propagating a model state X from the current time t to the new time $t + \Delta t$ (equation (1)). The model operator M of ICON is implemented in

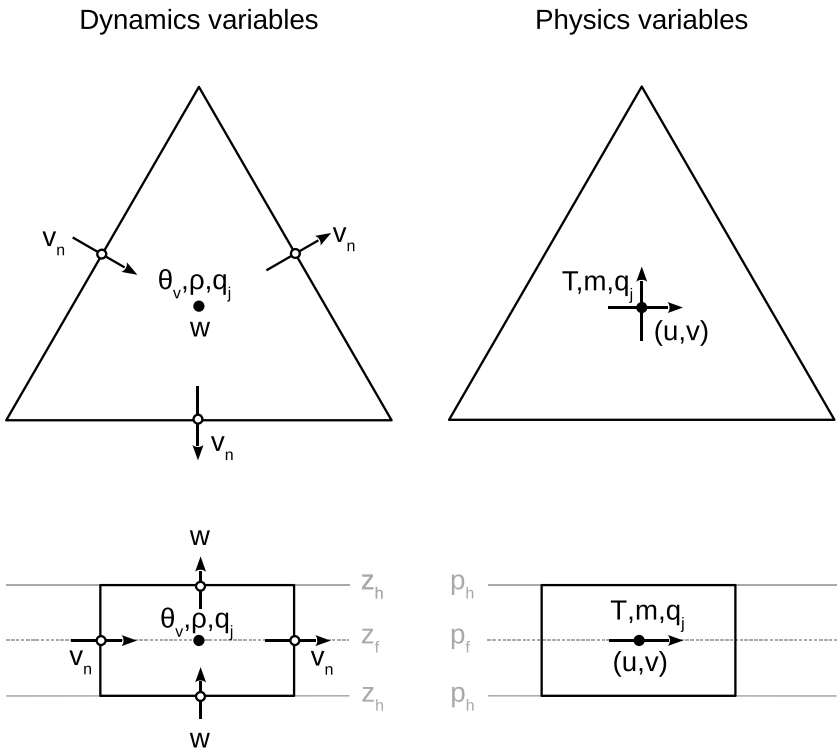

Figure 4. Distribution of the atmospheric state variables of (left column) the dynamics and (right column) the physics (top row) in a triangular cell and (bottom row) in the vertical plane. The vertical wind is not used in the physics.

separate operators for dynamics, tracer advection, and physics, which can be applied sequentially, as expressed by the white circle symbol in equation (2), or independently on the same state as indicated by the plus symbol between operators in equation (2). Figure 5 provides an overview of the whole procedure that is discussed in the following.

The dynamics that acts on the variables v_n, θ_v, and ρ is split in two parts, D_1 and D_2, of which D_1 is first applied n times in substeps of length Δt_{dyn}, followed by D_2 (equation (2)). The substepped dynamics D_1 includes advection of dynamical fields, pressure gradient, and Coriolis effects and a part of the physical forcing, F_1 (equation (3)), that was computed after the dynamics of the previous time step. Then the D_2 operator (equation (4)) applies diffusion and damping, as detailed in Zängl et al. (2015). The advection operator A (equation (5)) propagates the tracer mass mixing variables q_i over the time step Δt. This is followed by an update using also here the first part of the physical forcing, F_1 (equation (7)).

At this point the physical forcing from all considered processes is computed, with its tendencies of dynamical variables as well as tracer variables. These tendencies are then sorted in two forcings, F_1 and F_2, of which F_1 (equation (6)) will be passed to the next time step and applied in D_1 as described above. The other part, F_2, however, will be directly used by the physics operators to update the dynamical variables as well as the tracer variables, which conclude a time step and yields the final new state $X(t + \Delta t)$.

$$X(t+\Delta \mathrm{t}) = MX(t) = X(t) + \Delta \mathrm{t} \cdot \frac{\partial X}{\partial t}(X(t), F) \tag{1}$$

$$M = P(F_2) \circ \left(P(F_{1T}) + A + D_2 \circ D_1^n(F_1)\right) \tag{2}$$

$$D_1(F_1)X = \left(X + \Delta t_{\mathrm{dyn}} \cdot \frac{\partial X}{\partial t}_{\mathrm{dyn1}}(X, F_1)\right) \tag{3}$$

$$D_2 X = \left(X + \Delta \mathrm{t} \cdot \frac{\partial X}{\partial t}_{\mathrm{dyn2}}(X)\right) \tag{4}$$

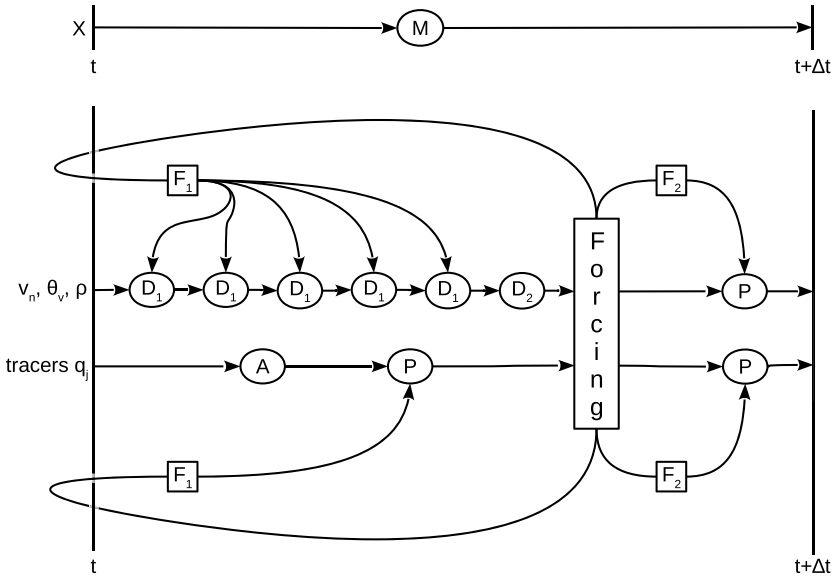

Figure 5. The model M propagates the state X from time t to the new time $t + \Delta t$ (upper part). The model operator M is split in operators for dynamics D, advection A, and physics P, which yield partial updates. The dynamical variables of X (v_n, θ_v, and ρ) are processed n times by the fast dynamics operator D_1, here shown for $n = 5$, followed by the damping/diffusion operator D_2. The fast dynamics can be forced by the forcing from slow physics, F_1. Tracer fields are first advected and then updated with the forcing from the slow physics. After dynamics, and tracer advection, including the slow physics forcing F_1, the forcing is newly computed, and the forcing owing to fast physics, F_2, is applied to dynamics variables as well as tracer variables.

$$AX = \left(X + \Delta t \cdot \frac{\partial X}{\partial t}_{\text{adv}}(X)\right) \tag{5}$$

$$F_1 = Tr_{\text{p2d}}\left(\frac{\partial Y}{\partial t}_{\text{phy1}}(Y)\right) \tag{6}$$

$$P(F_{1/2})X = X + \Delta t \cdot Tr_{\text{p2d}}\left(\frac{\partial Y}{\partial t}_{\text{phy1/2}}(Y)\right) \tag{7}$$

For the decision which physical processes to apply through F_1 or F_2 the following can be considered. When applying a physical forcing in the substepped dynamics, the dynamics can respond in smaller steps to the imposed forcing, but the forcing can only adjust at the longer intervals Δt to the changed state. Therefore, only a small number of dynamical substeps should be used. When applying a physical forcing after dynamics and advection, the forcing responds immediately to changes of the dynamics, but the dynamics has to respond to larger forcing increments.

The model configuration described by Zängl et al. (2015) divides the total forcing in a "slow physics" forcing comprising small and numerically uncritical tendencies, which is directly applied in the substepped dynamics, with $F_1 = F_{\text{slow}}$, and a "fast physics" forcing comprising the numerically more challenging tendencies to be evaluated and applied in a specific sequence after dynamics and advection, with $F_2 = F_{\text{fast}}$. Radiation contributes, for example, to F_{slow}, while cloud microphysics contributes to F_{fast}. For more details see Zängl et al. (2015).

For the AMIP experiments presented here a simplified variant of the general coupling scheme (equation (2)) is used, which computes the dynamics adiabatically, that is, $F_1 = 0$, and the complete physical forcing is evaluated and applied as F_2 after dynamics and advection (equation (8)). This corresponds to the dynamics physics coupling used in the ECHAM general circulation models.

$$M = P(F_2) \circ \left(A + D_2 \circ D_1^n(0)\right) \tag{8}$$

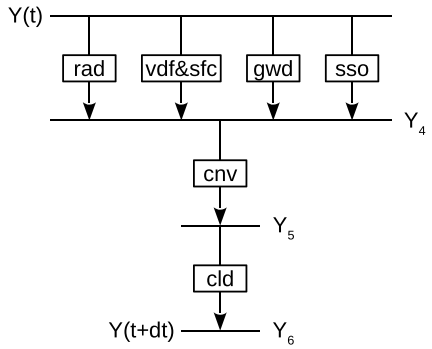

Figure 6. Process splitting in the ICON-A physics: radiation, vertical diffusion with surface processes, gravity wave drag, and subgrid-scale orographic effects are used in a parallel split method. These initial four processes and convection and cloud processes are serially split.

3.3. Physics Coupling

The forcing of the model dynamics includes physical and unresolved dynamical processes, which are combined in the "physics." In ICON-A the physics package includes (1) radiative effects by terrestrial longwave and solar shortwave radiation, (2) vertical diffusion with implicitly coupled land surface processes, (3) atmospheric gravity wave drag, (4) subgrid-scale orographic effects, (5) cumulus convection, and (6) cloud microphysics. These parameterizations are described in section 4. As the contributions of these processes to the forcing are parameterized separately, there remains the question of how to couple the processes to the dynamics and to each other. The choice of the scheme affects the numerical stability and the conservation properties of atmospheric general circulation models, as discussed by Williamson (2002) and Dubal et al. (2004, 2005). The parallel split method—using the terminology of Dubal et al. (2004), but also known as process split method—provides each parameterization with the same final state from the dynamics as input. Here the total forcing is simply the sum of the tendencies of the processes (equation (9)). The serial split method—also known as time-splitting method—allows the direct coupling between subsequent processes, however, with many options for the ordering of the processes. Here the atmospheric state needs to be updated between the processes before summing up the tendencies (equation (10)). This serial coupling provides the base for the conservation of tracer mass that can be jeopardized in the parallel split method if, for instance, moist convection and cloud processes together consume more water vapor over the length of the time step than available in their common input state.

For the ICON-A model a "mixed" scheme is used that combines the serial split and the parallel split method (Figure 6). This scheme consists of a serial splitting between an initial set of four parallel split parameterizations and two remaining parameterizations. The parallel split part combines radiation, vertical diffusion, and the gravity wave processes, thus providing smoothed final states of the dynamics to the parameterizations of these processes. The serial split puts the processes acting on tracer mixing ratios into a sequence in order to allow the conservation of tracers. Specifically, this serializes vertical diffusion, convection, and cloud microphysics. A comparison of different physics coupling schemes in ICON-A will be presented in a separate study.

$$\frac{\partial Y}{\partial t}_{\text{phy,par}}(Y) = \sum_j \frac{\partial Y}{\partial t_j}(Y) \tag{9}$$

$$\frac{\partial Y}{\partial t}_{\text{phy,ser}}(Y) = \sum_j \frac{\partial Y}{\partial t_j}\left(Y_{j-1}\right), Y_j = Y_{j-1} + \Delta \mathrm{t} \cdot \frac{\partial Y}{\partial t_j}, Y_0 = Y \tag{10}$$

3.4. Timing of Physical Processes

Physical processes act at a wide range of time scales. On these grounds and based on the necessity to make economic use of the computational resources, it is useful to have control on the time intervals in which the forcing of specific processes is recomputed. It is, for instance, very common to compute the radiative transfer—owing to the high computational costs—on much longer intervals than the forcing by other processes. ICON-A allows to define for each process P_j from the list enumerated above the date-time interval $[t_{\text{start}}(P_j), t_{\text{end}}(P_j)[$, within which the forcing is computed and applied in the time integration, as well as the interval $\Delta t(P_j)$, at which the forcing by process P_j is newly computed. The $\Delta t(P_j)$ must be a multiple of Δt. Thus, the forcing by process P_j is computed for the first time at the first model date time in the interval $[t_{\text{start}}(P_j), t_{\text{end}}(P_j)[$, and from then on in intervals $\Delta t(P_j)$. At all other model time steps the previously computed forcing is recycled. For model date/time outside the interval $[t_{\text{start}}(P_j), t_{\text{end}}(P_j)[$ the process has no effect at all.

In the AMIP experiments the physical processes are applied over the complete duration of the experiment, and recomputed every time step $\Delta t = 600$ s, except for radiation, where the radiative transfer is recomputed only with $\Delta t_{\text{rad}} = 7{,}200$ s.

Table 2
Key Physical Processes in ICON-A

Process	Base reference	Characteristics	Atm. tendencies
Cloud cover	Sundqvist et al. (1989)	Cloud cover diagnosed from relative humidity	–
RadiationSW and LW	"PSrad,"Pincus and Stevens (2013)	Correlated-k scheme, two streams, originating from RRTMG, scattering in SW, McICA for cloud effects	$\partial T/\partial t$
Vertical diffusion	Mauritsen et al. (2007)	Total turbulent energy scheme, implicitly coupled to the land surface model	$\partial T/\partial t$, $\partial q_{v,c,i}/\partial t$, $\partial u/\partial t$, $\partial v/\partial t$
Land surface	"JSBACH4-lite," Raddatz et al. (2007)	Five layers for water and heat storage, one surface type per cell	-
Cumulus convection	Nordeng (1994)	Mass flux scheme with shallow, deep or midlevel convection. Moisture convergence closure for shallow and mid level convection, CAPE closure for deep convection	$\partial T/\partial t$, $\partial q_{v,c,i}/\partial t$, $\partial u/\partial t$, $\partial v/\partial t$
Stratiform clouds	Lohmann and Roeckner (1996),	Prognostic cloud water and ice; diagnosed liquid or snow precipitation	$\partial T/\partial t$, $\partial q_{v,c,i}/\partial t$
Orographic drag	Lott (1999)	Orographic blocking and orographic gravity wave drag, subgrid-scale orographic parameters based on GLOBE elevation data	$\partial T/\partial t$, $\partial u/\partial t$, $\partial v/\partial t$
Nonorographic gravity wave drag	Hines (1997)	Spectra in eight azimuths, constant, globally uniform and isotropic wave sources at ~680 hPa	$\partial u/\partial t$, $\partial v/\partial t$

Note. The last column shows the tendencies in atmospheric variables resulting from each parameterization. The $\partial q_{v,c,i}/\partial t$ stands for tendencies of water vapor, cloud liquid, and cloud ice mass mixing ratios, respectively.

3.5. From Heating to Temperature Tendencies

Within the physical processes, where a pressure-based vertical coordinate is used, the specific heat of air at constant pressure c_p is used to convert the heat gain or loss to a temperature tendency. Thus, the mechanical work is implicitly accounted for in the updating for the provisional states Y_j between sequentially computed physical processes.

At the end of the physics computations the heating/cooling in units of W/m^2 that was accumulated from all processes is converted to a temperature tendency for constant volume conditions by using the specific heat of air at constant volume c_v. This temperature tendency is used subsequently to update the prognostic model state. The mechanical work for expansion or contraction in response to the local heating will then be simulated explicitly by the dynamics.

4. Physical Parameterization Package

The parameterizations for the physical processes are adopted from ECHAM6 (Giorgetta, Roeckner, et al., 2013; Stevens et al., 2013) more specifically from ECHAM6.3, which is the latest version of the ECHAM6 model line. The main documentation of ECHAM6, related to version 6.1 that was employed for CMIP5, is given by Stevens et al. (2013) and Giorgetta, Roeckner, et al. (2013). Subsequent developments aimed at the elimination of bugs causing energy leakages, which lead to ECHAM6.2. However, this version was not released due to an unrealistically high climate sensitivity. Further developments include the implementation of the PSrad radiation scheme with Monte Carlo independent column approximation for cloud radiative effects, the new simple-plume anthropogenic tropospheric aerosol climatology tropospheric, a five-layer soil hydrology scheme, more detailed land processes, and a new tuning lead to ECHAM6.3 that is employed for CMIP6. These changes are presented in brief in the following sections, except for the more detailed land processes, which are not yet used in this version of ICON-A. Beside these developments, ICON-A also makes use of a modified version of the vertical diffusion scheme, now formulated in total turbulent energy instead of turbulent kinetic energy, also described below.

Table 2 lists key physical processes that are represented in the model together with the variables, for which tendencies are computed and used as F_2 forcing in this model setup (cf. Figure 5). More details are compiled in the following sections.

4.1. Atmospheric Mass

In the hydrostatic ECHAM6 the mass of air in atmospheric layers is directly obtained from the layer pressure thickness Δp defined by the hybrid sigma-pressure vertical coordinate of ECHAM6. The ECHAM6 physics adopted in ICON-A, however, is modified in this aspect, and computes atmospheric mass from the density

ρ and geometric thickness Δz that is defined by the hybrid sigma-height vertical coordinate of ICON. Thus, the mass field of the dynamics can directly be used in the physics, instead of diagnosing it from a diagnosed hydrostatic pressure field.

4.2. Radiation

The solar shortwave and terrestrial longwave radiative heating is parameterized using the PSrad scheme of Pincus and Stevens (2013). This scheme implements the Rapid Radiation Transfer Model (RRTM) gas optics and solvers (Iacono et al., 2008, Mlawer et al., 1997) common in many other models, but was restructured and largely rewritten to allow different sampling strategies in its integration. The RRTM optics solves for the long-wave irradiances in 16 bands containing a total of 140 quadrature points (so-called g-points) in the wavenumber range between 10 and 3,250/cm. The shortwave radiative transfer is solved with 112 quadrature points over 16 bands spanning the wavenumbers between 820 and 50,000/cm. Multiple scattering is accounted for in the shortwave irradiance calculation, but not in the longwave. Thermal emission is central to the longwave calculation, but negligible (and neglected) in the calculation of shortwave irradiances.

In the ICON implementation of PSrad cloud effects are treated by sampling subcolumns, similar to Räisänen and Barker (2004) using a generalization of the Monte Carlo Independent Column Approximation (McICA; Pincus et al., 2003). This is performed by drawing independent realizations of the cloud fields for each g-point integral using a maximum random overlap assumption and the profile of cloud fraction calculated by the cloud scheme. Cloud optical properties are prescribed, using look-up tables derived from Mie calculations following the description for ECHAM6 (Stevens et al., 2013). The McICA treatment of clouds fixes an error in the treatment of partially cloudy atmospheres that was present in the ECHAM6.0 implementation of radiative transfer, although in the case of ECHAM6 this bug had only a minor influence because of a compensating bug that restricted cloud fractions to be either zero or one at a given time step.

The original PSrad has the capability to perform Monte Carlo Spectral Integrations (McSI; Pincus & Stevens, 2009), which allows more frequent radiation updates by calculating the fluxes by randomly selecting subspaces of the spectral domain. However, the PSrad implementation in ICON no longer includes the McSI, in favor of higher computational efficiency, and uses instead the full radiative transfer, albeit at lower frequency than the other processes related to the high computational costs, as used in ECHAM6. For the R2B4 resolution discussed here the radiation time step is $\Delta t_{\mathrm{rad}} = 2$ hr.

For shortwave irradiances, the incoming solar flux is computed for the proleptic Gregorian calendar and the parameterized VSOP87 orbit (for details see section B in Giorgetta, Roeckner, et al., 2013). Shortwave irradiances are calculated to be valid for the cosine of the solar zenith angle, μ, determined as the maximum between its value at that location at the midpoint time between two radiation time-steps and a minimum value, and then rescaled by the actual cosine of the solar zenith angle at the model time step. This rescaling facilitates treatment of irradiances at the terminator on time steps between radiation time steps and results in a smoothly varying diurnal cycle in solar heating, though cloud effects are spatially fixed and optical paths are no longer fully consistent with the solar zenith angle used for the incoming solar flux. The upward longwave irradiance from the surface is also corrected, by subtracting the surface blackbody emission at the time of the radiation time step and adding the surface blackbody emission at the model time step, to account for the change in surface temperature through the course of the radiation time step.

The externally specified annual mixing ratios of CO_2, CH_4, N_2O, and CFC11 and CFC12 are interpolated linearly in time between the next midpoints of years to the date and time of radiative transfer calculations. Similarly, the externally specified monthly and spatially varying ozone concentrations and aerosol optical properties are interpolated in time between the next midpoints of months.

While CO_2 and the CFCs are prescribed with homogeneous mixing in the whole model atmosphere, the mixing ratios of CH_4 and N_2O are reduced in the middle atmosphere near specified heights and with specified decay scale lengths to mesospheric background values, to mimic the mean effects of atmospheric chemistry on the vertical profiles of these two species.

4.3. Vertical Diffusion

Vertical transport by subgrid-scale turbulent motion is parameterized as turbulent diffusion. In ICON the turbulent kinetic energy scheme of Brinkop and Roeckner (1995) used in ECHAM is replaced by a total turbulent

energy scheme first proposed for modeling stably stratified conditions by Mauritsen et al. (2007). The scheme was later extended to convectively unstable conditions, implemented into the regional Weather Research and Forecasting model, and tested against large eddy simulations and observations (Angevine et al., 2010). Subsequently, the scheme was implemented into a version of global ECHAM6 model (Pithan et al., 2015), whereby the convective mass-flux part introduced by Angevine et al. (2010) was omitted to avoid double-counting with ECHAM6's existing convective mass-flux parameterization scheme.

The total turbulent energy, $E = E_k + E_p$, is the sum of turbulent kinetic (E_k) and turbulent potential energy (E_p). The latter is proportional to temperature variance. The prognostic budget equation for the total turbulent energy is

$$\frac{DE}{Dt} = \tau \cdot S - \gamma - \frac{dF_E}{dz} + \begin{cases} 0 & \text{for } Ri \geq 0 \\ 2B & \text{for } Ri < 0 \end{cases} \tag{11}$$

where τ is the turbulent stress vector, S is the vertical wind shear vector, γ is the turbulent energy dissipation, F_E is the diffusive vertical turbulent energy transport, Ri the gradient Richardson number, and B the turbulent buoyancy production, which is positive in unstable conditions ($Ri < 0$). A strength of the total turbulent energy approach is that under stably stratified conditions (Ri > 0), there is no buoyancy destruction term, and therefore, the scheme has positive net production of total turbulent energy whenever wind shear is present. Closure is obtained by linking total turbulent energy to turbulent fluxes through empirical Ri-based stability functions (Mauritsen & Svensson, 2007) and by defining a turbulent length scale (l):

$$l^{-1} = \frac{1}{\kappa z} + \begin{cases} \dfrac{2\Omega}{C_f\sqrt{\tau}} + \dfrac{N}{C_N\sqrt{\tau}} & \text{for } Ri \geq 0 \\ \dfrac{3}{\kappa(h_d - z)} & \text{for } Ri < 0 \end{cases} \tag{12}$$

where $\kappa = 0.4$ is the von Karman constant, Ω is the planetary rotation rate, N is the Brunt-Väisälä frequency, h_d is the depth of the convectively unstable boundary layer, and C_f and C_N are parameters. When the boundary layer is convectively unstable, the case for $Ri < 0$ is used below the entrainment zone in the upper part of the boundary layer wherever the stable branch yields larger mixing lengths. The scheme is extended to the near-surface layer where profiles of wind and temperature are approximated as logarithmic. This approach ensures consistent fluxes between the lowermost atmospheric layers. The turbulent heat flux from the surface, $w'\theta'$, is inversely proportional to the neutral limit Prandtl number Pr_0 (Eq. 20 in Pithan et al., 2015), which is set to 0.8 in ECHAM6.3. Pr_0 is used for the tuning of ICON-A, as described later.

4.4. Land Surface

The physical properties of the land surface, and the storage and land-atmosphere fluxes of heat and water are simulated by JSBACH v4, which is the new land component of ICON-ESM/ICON-A and the successor of JSBACH v3. JSBACH v3 has been and is used as the standard land component of MPI-ESM/ECHAM in past and current Coupled Model Intercomparison Projects (Giorgetta, Jungclaus, et al., 2013; Stevens et al., 2013). JSBACH v4 is a complete reimplementation of JSBACH v3 suitable for ICON and allowing a more flexible description of land surface heterogeneity through a hierarchical representation of surface tiles and their related processes.

The initial implementation used here is a "lite" configuration, which includes only the essential physical processes ported from JSBACH v3 (cf. Raddatz et al., 2007). Only a single vegetated tile is used in each land cell in addition to tiles for lakes and glaciers. Leaf area index and the ratio of vegetated to vegetation-free land are interpolated from a monthly climatology based on Version 2.0 of the U.S. Geological Survey Global Land Cover Characteristics Database (Hagemann, 2002). As in previous model versions, the surface energy balance and five thermal soil layers are implicitly coupled to the vertical diffusion scheme of the atmosphere. In contrast to the JSBACH v3 used in CMIP5, a five-layer soil hydrology scheme is used for the prognostic computation of soil water storage (Hagemann & Stacke, 2015).

4.5. Cumulus Convection

The convection scheme predicts either shallow, midlevel, or deep convection in one grid box using a bulk entraining-detraining plume. Shallow convection is closed on boundary layer moisture convergence, whereas a closure on the convective available potential energy (CAPE) is used for deep convection. The

strength of midlevel convection is related to the large-scale vertical velocity at cloud base. The convection scheme is formally based on the Tiedtke (1989) mass flux scheme including updates by Nordeng (1994). The implementation and characteristics of the scheme are as described in detail by Möbis and Stevens (2012) for the ECHAM 6.0 version, up to two differences. The differences are first that bugs related to phase changes of water have been fixed to ensure energy conservation in the convection scheme. These bug fixes already happened with the release of the ECHAM 6.1 model version. Second, several parameters of the convection scheme are used as tuning parameters (see Mauritsen et al., 2012) and thus exhibit distinct values in ICON-A and ECHAM6. To mention here are in particular the values of the turbulent entrainment rates, which are set to 0.2/km for deep and midlevel convection, 0.4/km for downdrafts, and 3/km for shallow convection in ICON-A, versus 0.1/km (deep and midlevel), 0.2/km (downdrafts), and 3/km (shallow) in the ECHAM 6.3 version. Further ICON uses a time scale τ_{mf} of 1 hr instead of 2 hr for the relaxation of the CAPE. Also, precipitation can form independently of the thickness of the convective cloud in ICON-A, which was not the case in ECHAM6 where a minimum thickness of 150 hPa over ocean and of 300 hPa over land was required. Finally, a nonphysical restriction of nondeep convection to $p > 400$ hPa, which practically limited the vertical extent of midlevel convection in ECHAM6, was removed. This threshold affected occasionally the convective tracer transport in the midlatitudes.

4.6. Stratiform Clouds

The scheme for the representation of stratiform clouds consists of prognostic equations for the vapor, liquid, and ice phase, respectively; a cloud microphysical scheme (Lohmann & Roeckner, 1996, with some revisions), and a diagnostic cloud cover scheme (Sundqvist et al., 1989).

The microphysical scheme models the conversion rates between water vapor, cloud water, and ice by several processes. Profiles of rain and snow rates are diagnosed in the columns, but not advected by the transport scheme. For a detailed documentation of all processes see section 2.6 in Giorgetta, Roeckner, et al. (2013).

The cloudiness profile $C(p)$ (equation (13)) is diagnosed following Sundqvist et al. (1989) from the relative humidity $r(p)$ and a critical relative humidity profile $r_0(p)$ (equation (14)), where r_{sat} defines the relative humidity for 100% cloud cover, that is, $C = 1$. The $r_{0,surf}$ is the critical relative humidity at the surface, $r_{0,top}$ is the asymptotic critical relative humidity in the upper troposphere, and n is a shape factor of $r_0(p)$. ECHAM6.3 and ICON use $r_{sat} = 1$, $n = 2$, and $r_{0,surf} = 0.968$. For $r_{0,top}$ ECHAM6.3 uses 0.75. In ICON $r_{0,top}$ is used for tuning purposes, see below, and finally set to $r_{0,top} = 0.8$.

$$C(p) = 1 - \sqrt{1 - \frac{r(p) - r_0(p)}{r_{sat} - r_0(p)}} \tag{13}$$

$$r_0(p) = r_{0,top} + \left(r_{0,surf} - r_{0,top}\right) \cdot e^{1-(p_s/p)^n} \tag{14}$$

4.7. Gravity Wave Parameterizations

Gravity waves are generally not explicitly resolved at the typical horizontal resolutions of a climate model. However, it is known that their transfer of momentum from the lower to the upper troposphere and higher up in the atmosphere is crucial to the large-scale circulation. Hence, gravity wave effects are usually parameterized. The gravity wave parameterizations in ICON are adopted from the ECHAM6 general circulation model for the atmosphere (Stevens et al., 2013). Two gravity wave parameterizations are used. One which take into account the momentum deposition from gravity waves generated only by orography as well as low-level orographic blocking effects, and a parameterization for the momentum deposition from gravity waves generated by transient phenomena within the atmosphere as, for instance, convection. While the former is considered in virtually all atmosphere general circulation models, the latter is typically included only in models with tops above the stratopause (Charlton-Perez et al., 2013) and is usually referred to as nonorographic gravity wave parameterization.

4.7.1. Orographic Gravity Waves and Blocking

The parameterization of these effects follows Lott and Miller (1997) and Lott (1999) and considers the drag exerted by the subgrid-scale mountains, when the airflow is blocked at low levels, and momentum transfer from the Earth to the atmosphere accomplished by orographic gravity waves. The propagation and dissipation of the orographic gravity waves follow wave-mean flow interaction theory (Andrews et al., 1987).

The parameterization depends on a statistical description of the subgrid-scale orography (SSO) within each cell. The scheme uses standard deviation of the elevation, anisotropy, slope, orientation, minimum, maximum, and mean elevation of the SSO (Lott, 1999). For ICON these parameters are derived from the global 30 arc sec resolved GLOBE elevation data (GLOBE Task Team et al., 1999), using the EXTPAR preprocessor (Smiatek et al., 2008) with extensions for icosahedral grids of the ICON models.

The current SSO parameters are somewhat compromised, because of two issues explained below, though still allowing to model the basic SSO effects. These problems will be addressed in the next version, when improved SSO parameters will become available.

The first issue concerns the SSO orientation parameter, describing the azimuthal angle of the long axis of elliptic mountains, which rotates toward 0°, indicating north-south orientation, with increasing latitude. The reason was identified in a missing accounting of the effects of the convergence of the meridians at the poles on the computation of the orientation angle. On a regular longitude latitude grid, as used for the GLOBE data, the convergence of meridians allows the representation of much higher metric zonal derivatives dh/dx than meridional derivatives dh/dy near the poles, which results in orientation angles rotating toward 0° near the poles (cf. eq. A.1 and A.2 in Lott and Miller (1997), unless preventive steps are taken.

The second issue concerns the elevation reference surface for the computation of the SSO standard deviation within a cell. In ICON the resolved surface is represented by a terrain following coordinate, thus allowing the dynamics to respond to resolved sloping terrain. However, the available SSO standard deviation is derived for a horizontal reference level. As a result, resolved sloping terrain can have substantial SSO standard deviations, depending on the steepness and grid scale. This issue is expected to affect mainly smoothly sloping regions over ice shields, in Antarctica and Greenland, where subgrid-scale elevation features are small, and is more severe for LR models than high-resolution models.

4.7.2. Nonorographic Gravity Waves

Multiple atmospheric sources of gravity waves, such as moist convection and fronts, are supposed to give rise to a broadband continuous spectrum of atmospheric gravity waves. The propagation and dissipation of such a gravity wave spectrum follow wave-mean flow interaction theory (Andrews et al., 1987) with the additional consideration of the gravity wave-induced wind perturbation in the gravity wave dissipation condition (Hines, 1997). Although the coupling of the propagation part of the parameterization to specific sources of gravity waves has been explored in previous ECHAM versions (Charron & Manzini, 2002; Schirber et al., 2014), here the standard approach used in ECHAM6 is applied, which means that space- and time-constant parameters for the gravity wave source spectrum have been used. Specifically, an isotropic spectrum with gravity wave wind speed of $\sigma_{TI} = 0.87$ m/s and effective horizontal wavenumber $K^* = 2\pi \cdot (126\ \text{km})^{-1}$ is launched from the lower troposphere, at about 680 hPa. This configuration has been chosen to allow direct comparisons with the ECHAM6 model. The treatment of gravity wave sources will be revised, following the experience we are accumulating, running ICON at convection permitting resolutions of ~2.5 km (Klocke et al., 2017).

5. Parameter Setting and Tuning

The parameterized forcing of the presented ICON-A model is in most parts inherited from the ECHAM6.3 model with only a few structural modifications, as described above. Also, the spatial resolution is chosen to be overall comparable, despite the obvious differences between the icosahedral grid of ICON and the longitude latitude grid used for physics in ECHAM6.3. Therefore, we assume that the basic parameter setting used in ECHAM6.3 should provide a reasonable starting point for AMIP simulations with ICON-A. Thus, the purpose of the tuning is to find parameter values, which overall provide a solution of similar quality. Ideally, a small number of tuning steps suffices.

The primary tuning goal—for ICON-A as for ECHAM6.3—is to obtain in the global annual mean a slightly positive downward net radiation flux at the top of the atmosphere (TOA) between 0 and 1 W/m^2, based on a net shortwave flux and an outgoing longwave radiation (OLR) close to observational estimates. This tuning goal is chosen to make the atmospheric model suitable for coupled climate simulations, for which large energetic unbalances at TOA would be detrimental. The primary means for this tuning consist in tunable parameters providing control on the amount and distribution of water vapor, cloud condensate, and cloud cover. Once a satisfactory setup is found, with respect to the radiative fluxes at TOA and the net planetary energy balance, then the dynamics is tuned by way of tunable parameters of the subgrid-scale orographic

Table 3
Tuning Parameters From Icon-aes-tune-1 to Icon-aes-tune-5 That is Equal to Icon-aes-1.3.00

Parameterization	Parameter	Units	Icon-tune-1	Icon-tune-2	Icon-tune-3	Icon-tune-4	Icon-tune-5
Convective clouds	ε_{mid}	m^{-1}	0.0001	**0.0002**	0.0002	0.0002	0.0002
	ε_{pen}	m^{-1}	0.0001	**0.0002**	0.0002	0.0002	0.0002
	ε_{dd}	m^{-1}	0.0002	**0.0004**	0.0004	0.0004	0.0004
	τ_{mf}	s	7200	**3600**	3600	3600	3600
Neutral limit Prandtl number	Pr_0	1	0.8	0.8	**1**	1	1
Cloud cover	$r_{0,top}$	1	0.75	0.75	0.75	**0.8**	0.8
Orographic blocking	C_d	1	0	0	0	0	**0.01**
Orographic gravity wave drag	G	1	0.05	0.05	0.05	0.05	**0.1**
Nonorographic gravity wave drag	σ_{TI}	m/s	0.87	0.87	0.87	0.87	0.87

Note. The setup of icon-tune-1 differs only in the orographic blocking and gravity wave tuning parameters from that of ECHAM6.3, due to the different underlying orographic data sets, see text. Changes of tuning parameters compared to the preceding experiment are indicated in bold. The nonorographic gravity wave drag parameter σ_{TI} has been tested with other values (see text) but remained unchanged.

blocking and gravity wave drag and the nonorographic gravity wave drag. The goal of this dynamical tuning is to reduce biases in the zonal ocean surface wind stress, again to support the usage of this model in coupled climate simulations, and further to reduce the zonal mean zonal wind biases in the troposphere and stratosphere. Sections 5.1 to 5.5 present the essential tuning experiments that lead on the most direct route, that is, in the smallest number of steps, from the initial ICON-A setup with ECHAM6.3 parameters to the presented ICON-A model. Additional tuning experiments, which were performed, for example, to explore the suitability of other parameters for the tuning goals, or to explore the sensitivity of target variables to the finally selected tuning parameter, are for brevity not reported. An overview of the parameter setting for the five tuning experiments, from icon-tune-1 that resembles the tuning of ECHAM6.3 to icon-tune-5 that was versioned as icon-aes-1.3.00, is given in Table 3.

5.1. ICON With Parameters From ECHAM6.3

Parameters for cloud cover, convective clouds, stratiform clouds, and the nonorographic gravity wave drag are set as in ECHAM6.3, specifically as in version ECHAM6.3 in the LR setup.

Parameters for the orographic blocking and gravity wave drag, however, differ because of the different underlying topographic data, as discussed above. At this stage the structural changes for the boundary layer turbulent fluxes, precipitation from shallow clouds, and the unlimited vertical depth of midlevel convection are already included. This setup is tested in the simulation icon-tune-1.

Comparing global and annual means of icon-tune-1 and ECHAM6.3 (Figure 7), the following is found: In icon-tune-1 the SW and LW radiative fluxes at TOA are both close to 240 W/m^2, as in CERES (version CERES-EBAF-Ed4.0; Kato et al., 2013; Loeb et al., 2009), with a small positive balance. These fluxes are ~2 W/m^2 stronger than in ECHAM6.3. The total cloud cover is larger in icon-tune-1, 64.5%, than in ECHAM6.3, 63.2%, but still substantially smaller than estimated by CERES. From this it may already be inferred that the clouds are reflecting the SW radiation more effectively, which can be the result of a high bias in higher clouds compared to lower clouds, as discussed in Crueger et al. (2018).

The vertically integrated water vapor in icon-tune-1 is by 0.6 kg/m^2 larger than in ERA-interim (Dee et al., 2011), and smaller by the same amount than in ECHAM6.3. This may be the effect of the changed boundary layer turbulence scheme. The lower water vapor path contributes to the increased outgoing LW radiation in icon-tune-1 compared to ECHAM6.3. The global mean precipitation in icon-tune-1 is 3 mm/day, which is 0.1 mm/day higher than in ECHAM6.3. The vertical integrals of cloud water and ice are 10% smaller than in ECHAM6.3.

5.2. Entrainment and Convective Relaxation Time Scale

Turbulent entrainment rates, as used in the convective parameterization for updrafts and downdrafts, are not observable, though cloud-resolving simulations have been used to estimate entrainment and detrainment rates (Baba, 2018; Siebesma & Cuijpers, 1995; Zhang et al., 2016). These studies typically find entrainment rates of $1 \cdot 10^{-3}$/m, which are about 1 order of magnitude higher than those used in convection parameterizations (Zhang et al., 2016). Nordeng (1994), for example, used a turbulent entrainment rate of $1 \cdot 10^{-4}$/m for

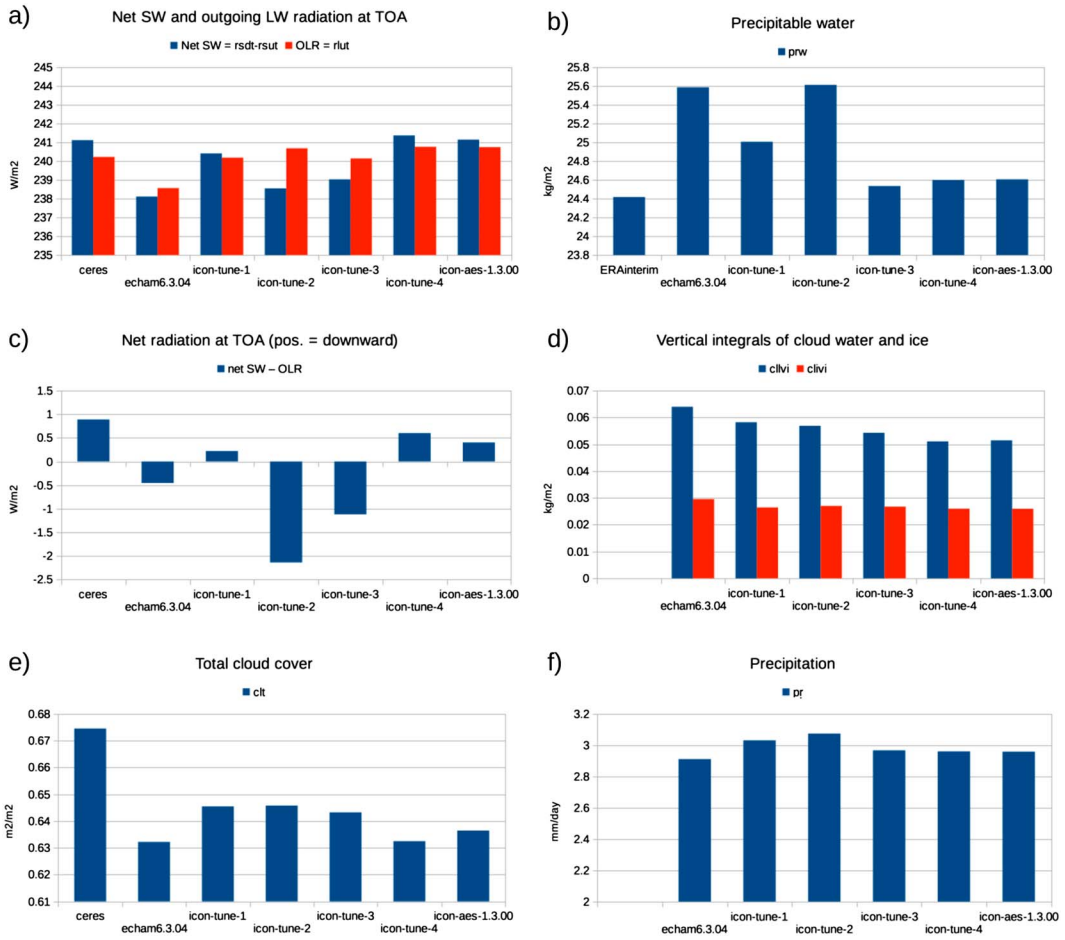

Figure 7. Global annual mean values of selected variables for reference data, ECHAM6.3 in LR configuration, and four ICON experiments from the model development process (icon-tune-1 to icon-tune-4) and the final version icon-aes-1.3.00. Variables displayed are (a) the net shortwave incoming and outgoing longwave fluxes at TOA, (c) the resulting net radiation at TOA, (e) total cloud cover, (b) the vertical integrals of water vapor, and (d) cloud water and ice, and (f) precipitation. CERES-EBAF-Ed4.0 from 2000/2003 to 2016/2002 is used as reference for radiative fluxes at TOA and total cloud cover. ERA-Interim is used as reference for precipitable water.

deep convection. In ECHAM6, Mauritsen et al. (2012) experimented with deep convection entrainment rates of $1 \cdot 10^{-4}$/m and $3 \cdot 10^{-4}$/m. Thus, also, for ICON-A, useful entrainment rates are expected to be of order 10^{-4}/m.

The relaxation time scale for the CAPE closure of the convection scheme is assumed to reflect the time scale of convective clouds, that is, order of 1 hr, and is believed to be sensitive to the horizontal resolution (Nordeng, 1994).

Here the entrainment rates for deep and midlevel convection and downdrafts are doubled, and the decay time scale of CAPE are halved compared to the values used in icon-tune-1 and ECHAM6.3. This modification follows ECHAM6-based experience that an intensified mixing between convective air and the environment, and a faster adjustment, is beneficial for the simulation of intraseasonal variability. These changes were adopted without regard to the effects. This setup is tested in experiment icon-tune-2.

The strengthened entrainment and shortening of the convective adjustment time primarily increase the water vapor path, from 25 to 25.6 kg/m^2, and decrease the net incoming SW radiation at TOA due to more reflected SW radiation. Water vapor path and net SW flux at TOA in icon-tune-2 have again similar values as in echam6-3-03-LR. The OLR in icon-tune-2 is only slightly stronger than in icon-tune-1. Cloud water and ice amounts, as well as the total cloud cover, are essentially unaffected. Due to the strong SW effects of the changes in icon-tune-2, the energy budget at TOA is changed from slightly positive to -2.1 W/m^2.

5.3. Turbulent Surface Fluxes and Moisture

The new boundary layer scheme is tunable by means of the neutral-limit Prandtl number Pr_0, which inversely scales the turbulent heat flux $w'\theta'$ from the surface. Kays (1994) estimated a range of 0.7 to 1 for Pr_0. Pithan et al. (2015) discussed how modifications of Pr_0 modify the boundary layer temperature profile, and in the tropics essentially the whole tropospheric temperature profile and through thermodynamics also the water vapor column. Specifically, Pithan et al. (2015) showed that a lowering of Pr_0 in their ECHAM6-TTE model resulted in a warming and moistening of the troposphere. Based on their findings and recommendations, the total turbulent energy scheme was implemented in ICON-A with $Pr_0 = 0.8$. As the water vapor path is too high in icon-tune-2, Pr_0 is increased here to $Pr_0 = 1.0$. with the goal to obtain a better agreement with the water vapor path in ERA-Interim analyses. This setup is tested in experiment icon-tune-3.

With this modification the global water vapor path is 24.6 kg/m^2, in better agreement with ERA-interim. As a side effect the cloud water path and the total cloud cover decrease slightly. Precipitation is now reduced to slightly less than 3 mm/day. The net SW flux at TOA is increased by ~0.4 W/m^2, while the OLR is reduced by ~0.6 W/m^2, so that the energy imbalance at TOA is halved to -1.1 W/m^2.

5.4. Reducing the SW Reflection

In icon-tune-3 the radiation at TOA is mainly biased in the SW component, because of too much reflection. This can be improved by reducing the cloud cover or the cloud brightness or both. In ICON the most direct way is to modify the vertical profile of the critical relative humidity by means of the critical relative humidity parameters for the surface, $r_{0,surf}$, and the upper troposphere, $r_{0,top}$ (equation (14)). These parameters are naturally bounded by the interval]0,1]. Sundqvist et al. (1989) used critical values of "near unity" at the surface and in the upper troposphere where cirrus clouds exist, and smaller values of 0.75 over land and 0.85 over sea in the middle troposphere. In ECHAM6, the critical humidity decays exponentially upward (equation (14)) with $r_{0,surf} = 0.968$ and $r_{0,top} = 0.75$. These values are clearly higher than the observational estimates by Quaas (2012), which indicates, for a 1° × 1° resolution, much lower values of ~0.4 in the middle troposphere and less than 0.6 in the upper troposphere (Figure 3 in Quaas, 2012). However, within the ECHAM model family, such low critical values do not allow realistic total cloud cover and TOA radiative fluxes. Thus, also in ICON-A $r_{0,top}$ must assume values above the range of Quaas (2012).

Given that ICON-A like ECHAM6 generally underestimates the cloudiness in the lower troposphere, but overestimates the cloudiness above, we tune here $r_{0,top}$ to reduce the cloudiness and thus the SW reflection. Thus, $r_{0,top}$ is increased in icon-tune-4 to 0.8.

As intended, the increase of $r_{0,top}$ reduces the cloudiness in the upper troposphere, leading to a decrease of the total cloudiness by 1% and a reduction of the SW reflection and increase of the net SW flux at TOA, of 2.3 W/m^2. As a side effect of less high cloudiness, the OLR is increased by a small amount. The resulting net radiation at TOA is +0.6 W/m^2, which is close to the CERES estimate of the Earth's energy imbalance, +0.9 W/m^2, and the recent estimate by Johnson et al. (2016) of +0.71 ± 0.10 W/m^2, and within the targeted range of 0 to +1 W/m^2.

5.5. Tuning Subgrid-Scale Dynamics

The finite horizontal resolution of a general circulation model, as presented here, can only insufficiently represent the dynamical effects of orography on the circulation. These effects include the blocking of the circulation by high mountains, which deflect the low-level circulation sideways, and the generation of gravity waves, if the circulation flows over an obstacle. Both effects are parameterized by the scheme of Lott (1999) dependent on the strength and direction of the circulation, the stability of the atmosphere, and a parametric description of the unresolved orography in a grid cell with at least fractional land surface. The parameters are the minimum, mean, and maximum height of the terrain in a grid cell; the standard deviation of the height, the slope, and the anisotropy; and orientation of mountains of an elliptic shape. Lott (1999) derived these parameters from the U.S. Navy (10′ × 10′) elevation data. Obviously, the resolution of the elevation data impacts the parameters describing the unresolved orography in a grid cell, and thus requires the scaling of the parameterized effects on the circulation by some dimensionless tuning parameters.

Lott (1999) provide dimensionless tuning parameters C_d and G for orographic blocking and gravity wave drag, respectively, which allow to tune the effects of these processes on the circulation, whether to reflect

Table 4
Parameterized Dynamical Processes (First Column), Related Tuning Parameters (Second Column), Parameter Values Used for Tuning (Third Column), and the Final Choice for Icon-aes-1.3.00 (Last Column)

Parameterization	Tuning parameter	Units	Test values	Icon-aes-1.3.00
Orographic blocking	C_d	1	0.01, 0.02, 0.05	0.01
Orographic gravity wave drag	G	1	0.02, 0.05, 0.10, 0.15	0.1
Nonorographic gravity wave drag	σ_{TI}	m/s	0.791, 0.87, 0.935	0.87

the resolution of the underlying elevation data, or other factors. Both parameters were expected to be of order 1, when used with orographic parameters derived from the U.S. Navy ($10' \times 10'$) elevation data. Setting C_d or G to zero would be equivalent to switching off the related process. For ICON the orographic parameters are derived from the more recent GLOBE elevation data with a resolution of $30'' \times 30''$ (~1 km × 1 km). The higher resolution results in more extreme minimum and maximum heights, higher standard deviations, and slopes, which requires smaller tuning parameters C_d and G, with typical values to avoid exaggerated effects.

The nonorographic gravity wave drag is tunable by the total root-mean-square gravity wave wind speed σ_{TI} at the source level, and the height of the source level H_I (cf. section 2.7.3 in Giorgetta, Roeckner, et al., 2013). As these parameters are used globally uniformly and constantly over time, they are not attributed to specific sources, like for example convective events, but represent sources in an average sense only. Here the gravity wave spectra are launched from the 10th level above ground that is at ~680 hPa and we assume a gravity wave wind speed of order of 1 m/s, as in ECHAM6. These settings were based on the experience gained on the sensitivity of the net momentum fluxes in the lowermost stratosphere to the launching height (Manzini & McFarlane, 1998), on the plausible range of the gravity wave variances estimated to be in the order of a few m/s (Fritts & Nastrom, 1992), and on the resulting absolute momentum fluxes, which agree within a factor of 2 with those derived by satellite observation in the lower stratosphere (Geller et al., 2013).

Here C_d and G are used for the tuning of the zonal wind stress on the ocean surface and, in conjunction with σ_{TI}, the zonal mean wind and temperature in the troposphere and stratosphere. As the three parameterized processes are sensitive to changes in the wind structure, the effects of the three processes combine nonlinearly, thus making a sequential tuning effort unpractical. Instead for each tuning parameter a small set of parameters was chosen (Table 4), and test experiments were performed for all combinations of the three parameters. From these 36 experiments the best one was chosen, based on a subjective selection. This selection was later confirmed by the statistical bias analysis detailed in Crueger et al. (2018). The selected simulation was tagged as icon-aes-1.3.00.

The selected scaling parameters for the SSO effects are $C_d = 0.01$ and $G = 0.1$. In ECHAM6.3-LR, for which the SSO parameters were derived from the coarser U.S. Navy ($10' \times 10'$) elevation data, the values are $C_d = 1.0$ and $G = 0.2$. Notable is that C_d must be set to a very small value, 100 times smaller than in ECHAM6.3. We suspect that this is related to the discussed issues in the preprocessing for the SSO parameters. The total root-mean-square gravity wave wind speed σ_{TI} for the nonorographic gravity wave effects was left unchanged compared to ECHAM6.3, at $\sigma_{TI} = 0.87$ m/s. Maps of annual mean biases related to the circulation are discussed below in comparison to ECHAM6.3.

5.6. Bias Maps for ECHAM6.3 and ICON-A

Figure 8 shows the time mean bias maps for the SW net flux at TOA, the OLR, and the water vapor path for the final ICON-A model, and for comparison the ECHAM6.3 model. These three variables were the main target of the tuning steps three and four. The model fields are averages for the initial 10 years of the AMIP experiments: CERES data for the available period 2001–2013 and ERA-interim for the full AMIP period, as used in Crueger et al. (2018).

For the SW net flux at TOA the equatorial negative bias is almost identical for both models. The subtropical positive bias of ECHAM6.3 is largely removed in ICON-A. The negative bias in the high-latitude southern oceans, however, is intensified in ICON-A. The OLR bias has the largest, positive deviations centered at the equator in the maritime continent, South America, and Africa. The center in the maritime continent is shifted toward the Indian Ocean in ECHAM6.3, but more toward the western Pacific in ICON-A. The South American

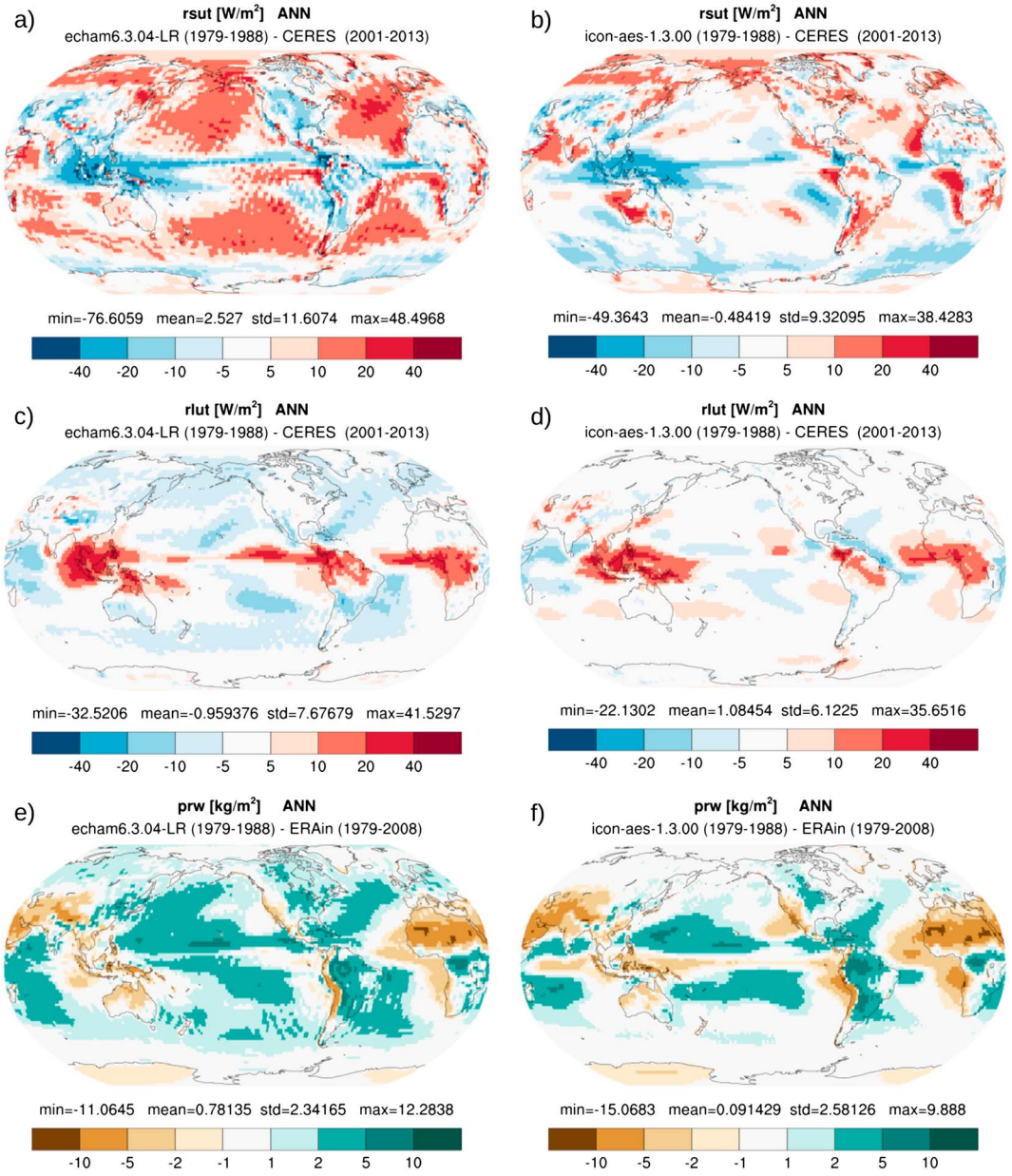

Figure 8. Climatological biases of 10-year AMIP simulations of (a, c, and e) ECHAM6.3 and (b, d, and f) icon-aes-1.3.00 for the reflected SW flux at TOA (a and b), the OLR (c and d), and the precipitable water (e and f). Reference data are from CERES-EBAF-Ed4.0 for the radiation and ERA-interim for water vapor.

bias is reduced in ICON-A, while little difference exists in the bias originating from Africa. The midlatitude negative biases of ECHAM6.3 are largely removed in ICON-A.

The water vapor path bias is mostly confined to the tropics, with the strongest moist bias over oceans and the strongest dry bias over subtropical continents, foremost in desert areas. The moist bias branches extending in ECHAM6.3 from the tropical western oceans eastward toward higher latitudes are reduced in ICON-A. By that also the high-latitude moist biases have disappeared, which in ECHAM6.3 relate to the OLR bias pattern.

The spectral ringing signature in the ECHAM6.3 biases for the net SW flux and the precipitable water result from the spectral representation of the dynamical fields. In ICON-A no obvious artifacts from the horizontal discretization of the dynamical core can be identified.

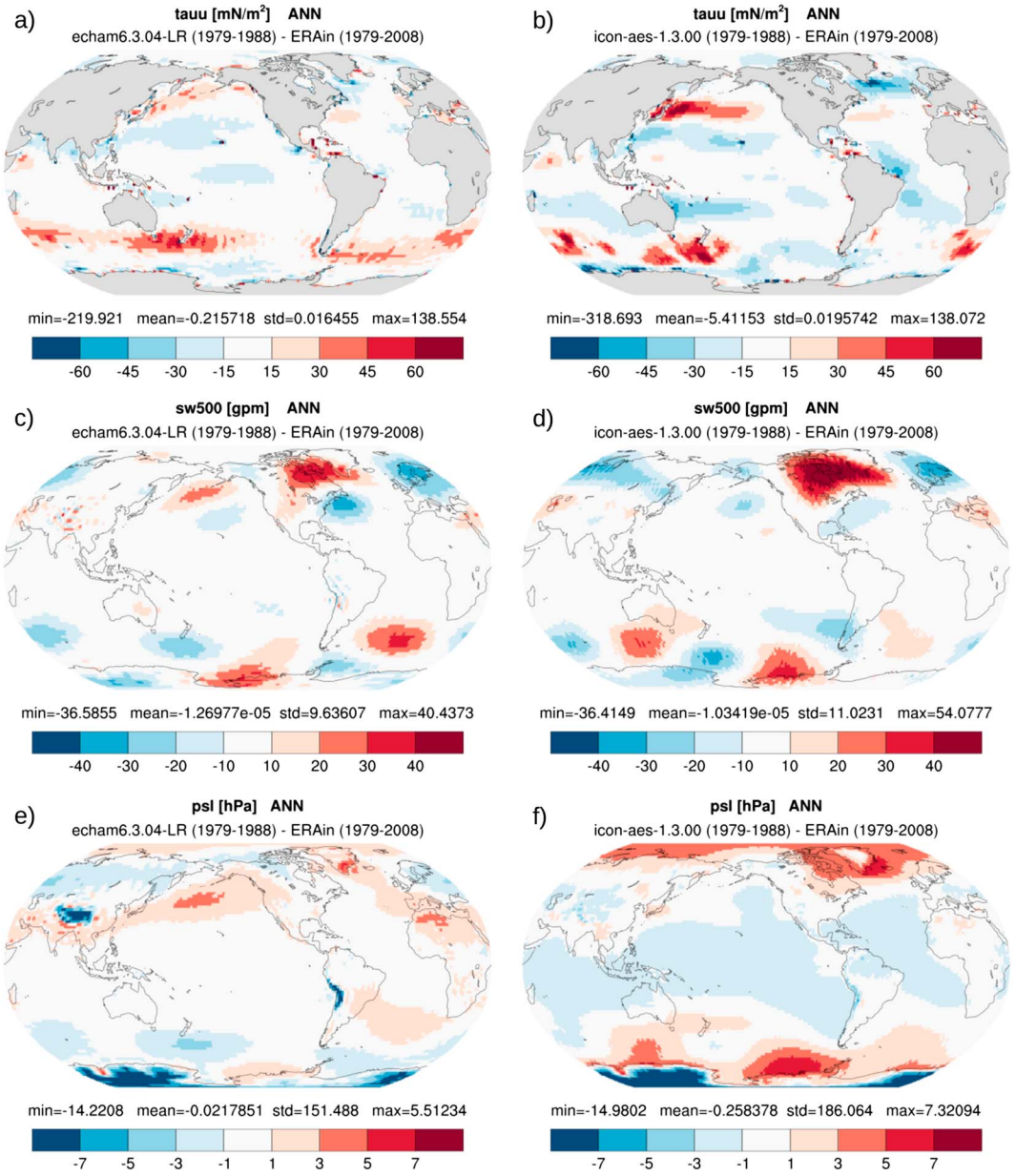

Figure 9. Climatological biases of 10-year AMIP simulations of (a, c, and e) ECHAM6.3 and (b, d, and f) icon-aes-1.3.00 for the zonal ocean surface wind stress (a and b), the stationary wave in the 500 hPa geopotential height (c and d), and the sea level pressure (e and f). Reference data are from ERA-Interim.

Figure 9 shows a comparison for dynamical fields, which are sensitive to the parameterized drags. In the zonal ocean surface wind stress τ_u (upper row), which was a priority for the tuning, ECHAM6.3 shows mainly a positive, that is, westerly bias in the high southern latitudes. This could be reduced in ICON-A, though regions of positive biases exist in particular south of Australia and South Africa. Further ICON-A features a zonally elongated positive bias in the northwestern Pacific. ECHAM6.3 shows only a weaker positive bias in the northwestern Pacific. ICON-A also exposes negative biased regions in the subtropical oceans, which hardly occur in ECHAM6.

In the biases of the stationary wave pattern of the geo-potential height at 500 hPa (middle row), which is indicative of the mid tropospheric circulation, the patterns are of similar amplitude in ECHAM6.3 and ICON-A. In both models the main bias occurs in North America, with a strong positive bias, and

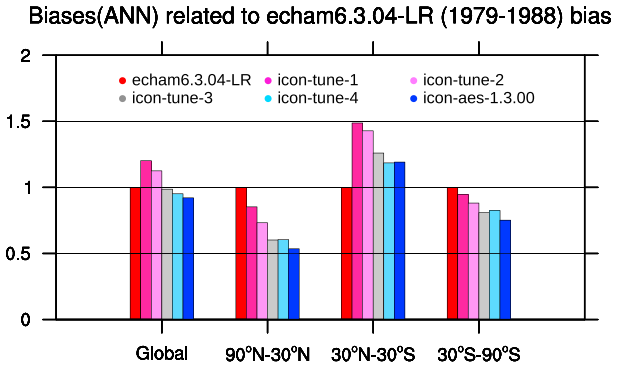

Figure 10. Multivariable biases of 10-year AMIP simulations of ECHAM6.3 (red), the intermediate ICON tuning versions, and the final version icon-aes-1.3.00 (blue). The biases are normalized such that ECHAM6.3 has a bias of value 1. Biases larger/smaller than 1 indicate larger/smaller biases than in ECHAM6.3. Biases are shown for the globe and 90°N–30°N, 30°N–30°S, and 30°S–90°S.

downstream in Scandinavia with a negative bias. In the southern hemisphere, both models have a positive bias west of the Antarctic peninsula, and a second positive bias in the South Atlantic in ECHAM6.3, and south of Australia in ICON-A. In general the mid tropospheric circulation seems of similar quality in ICON-A and ECHAM6.3. This holds also for the zonal mean wind and temperature as discussed in Crueger et al. (2018).

In the sea level pressure (bottom row), the bias patterns differ clearly between the models. ICON-A shows a negative bias in most of the tropics and compensating positive biases in the Arctic and in the southern oceans. These widespread biases in sea level pressure in ICON-A result from the prioritization of the zonal ocean surface wind stress and of the zonal mean wind and temperature structure over the sea level pressure. Better result for the seal level pressure were found for some of the SSO tuning experiments, though at the price of larger and less acceptable biases in the zonal ocean surface wind stress or the zonal wind and temperature structure.

Overall the dynamics tuning of ICON-A is only partially successful. We assume that corrected SSO parameters will allow an improvement in the representation of the orographic effects on the circulation, including the latitudinal mass distribution.

5.7. Multivariable Bias Statistics

For an overall assessment of the mean state of the tuning experiments, we utilize a performance index motivated by Reichler and Kim (2008) and Watterson et al. (1999) and utilized by Stevens et al. (2013). This is based on a comparison of the annual climatology of single variables with satellite- or reanalysis-based estimates of the true climatology, as further detailed in the companion paper by Crueger et al. (2018). This assessment also scales the biases of the tuning experiments by the biases of a reference experiment, for which we use here the ECHAM6.3 simulation. Thus, resulting bias indices larger or smaller than 1 indicate larger or smaller biases in the tuning simulation than in the ECHAM6.3 simulation.

Figure 10 shows that simply transferring the parameters from ECHAM6.3 to ICON-A, as in icon-tune-1, increases the bias by 20%. The same moderate increase is found in a comparison of the ECHAM6.1 simulations for CMIP5 (Stevens et al., 2013) to the ECHAM6.3 simulation. For all following tuning simulations—icon-tune-2 to icon-tune-4—and icon-aes-1.3.00 the global overall scores decrease. The final bias is 10% better than in the reference simulation. The biggest bias reduction results form the third step targeting the atmospheric water vapor path.

The regional biases show how the overall biases in the ICON simulations are larger in the tropics, where initially the bias increased by 50% compared to the ECHAM6.3 simulation. This increase could only partially be compensated in the following tuning steps. As discussed in Crueger et al. (2018) this primarily results from displaced oceanic precipitation bands, and further from the subtropical surface wind stress. In the extratropics all ICON simulations behave better than ECHAM6.3, especially in the northern hemisphere where the overall bias is reduced by 50%.

5.8. Remaining Issues

The tuning of ICON-A failed to resolve some issues, which will have to be addressed in the future, by better resolution, improved formulation of processes, more skillful tuning, or by better external data. These issues include the organization of the tropical precipitation, especially in the intertropical convergence zones in the Pacific, as discussed by Crueger et al. (2018), most likely originating from the interaction of parameterized convection and the resolved dynamics. Especially the parameterized entrainment/detrainment should be revisited.

Second, the vertical distribution of clouds is biased, with a strong underrepresentation of shallow clouds in the tropics and an overrepresentation of middle and upper tropospheric cloudiness in the middle and equatorial latitudes. This is a long-standing problem, which may originate from cloud microphysics as well as entrainment/detrainment of midlevel and deep convection.

Third, the circulation in the stratosphere and mesosphere is biased, especially in the winter hemisphere, where too much drag is exerted. It is felt that this problem is associated with the parameterization of the SSO drag. It is expected that the corrected SSO parameters can be utilized in future ICON-A versions to reduce the biases in the stratospheric and mesospheric circulation biases, and in the sea level pressure.

6. Conclusions

Within the ICON framework the ICON-A model has been developed for the future employment in the ICON-ESM for global climate research. The model presented here is focused on the uncoupled AMIP experiment as a prerequisite for coupled experimentation. ICON-A uses the nonhydrostatic dynamical core, as used in the current operational numerical weather prediction at the German Weather Service (Zängl et al., 2015) and in the large eddy resolving regional process studies of Heinze et al. (2017). ICON-A, however, differs from the model configurations for numerical weather prediction and large eddy simulations in the physical parameterization packages. For ICON-A the physics package originating from the ECHAM6 model (Stevens et al., 2013) has been adopted with a small number of modifications. Also, the coupling between the dynamics and physics resembles that used in ECHAM6.

This model was tuned on the base of the first decade of the AMIP experiment (1979–1988), starting from the tuning parameters of the ECHAM6 version in the "LR" setup that is overall comparable to the ICON-A setup used here. The primary tuning target are the global and time averaged net shortwave and OLR, and close-to-zero net energy flux, at the top of the model atmosphere, as required for the future employment in the coupled ICON-ESM. Further, attention was payed to the precipitable water, zonal wind stress at the surface, and the zonal mean wind and temperature.

The tuning of the subgrid-scale orographic blocking and gravity wave drag, and the nonorographic gravity wave drag, turned out to be problematic, related to issues in the preprocessing of the SSO parameters for the orientation angle and the standard deviation. These issues need to be addressed in a future version when the corrected SSO parameters are available.

Overall it is found in this work and in the accompanying evaluation by Crueger et al. (2018) that the new ICON-A model performs at a comparable level as the latest ECHAM6 version, with disadvantages in the tropics and advantages in the extratropics. We assume therefore that the transfer of the physics package from ECHAM to ICON was successful. However, for general circulation models as the ICON-A model, no proof can be given that the model is free of errors or bugs in the parts of the model that are used in the AMIP experiment. In the course of the development errors and bugs entered the code, leading to unexpected, nonphysical, or technically incorrect results, which triggered a search and eventual correction. The satisfactory comparison of ICON-A and ECHAM6 thus suggests that remaining, undetected errors or bugs in ICON-A have relatively small effects, or, if present in ECHAM and ICON, have similar effects.

The completion of the development of the ICON-A model on the basis of the AMIP experiment now opens up the employment of ICON-A as atmospheric component in the ICON-ESM, and the development toward high-resolution model configurations, where the nonhydrostatic formulation and the option to use massive parallelization provided by the ICON modeling system become important.

Acknowledgments
The Max Planck Society for the Advancement of Science is thanked for their support of this research. Computational resources were made available by Deutsches Klimarechenzentrum (DKRZ) through support from the Bundesministerium für Bildung und Forschung (BMBF). Computations were carried out at the German Climate Computing Center/ Deutsche Klimarechenzentrum (DKRZ) on the "Mistral" super computer. The ICON model is developed in collaboration between MPI-M and the German Weather Service/Deutscher Wetterdienst (DWD), where the ICON project was initiated by Guy Brasseur and Detlev Majewski, respectively. Florian Prill at DWD and Leonidas Linardakis at MPI-M developed important parts of the ICON model infrastructure. CERES data were obtained from the NASA Langley Research Center CERES ordering tool at http://ceres.larc.nasa.gov/. ERA-interim data sets are available from ECMWF (http://apps.ecmwf.int/datasets/data/interim-full-daily/). T. C. has received funding through the Climate System Analysis and Prediction excellence cluster at the University of Hamburg supported by the German Science Foundation. M. S. was supported by the Hans-Ertel Centre for Weather Research, which is funded by the Federal Ministry of Transport and Digital Infrastructure (BMVI). Primary data used in this work are archived by the Max Planck Institute for Meteorology and made available by contacting publications@mpimet.mpg.de.

References

Andrews, D. G., Holton, J. R., & Leovy, C. B. (1987). *Middle atmosphere dynamics* (p. 489). New York: Academic.

Angevine, W. M., Jiang, H., & Mauritsen, T. (2010). Performance of an eddy diffusivity-mass flux scheme for shallow cumulus boundary layers. *Monthly Weather Review*, *138*(7), 2895–2912. https://doi.org/10.1175/2010MWR3142.1

Baba, Y. (2018). Spectral cumulus parameterization based on cloud-resolving model. *Climate Dynamics*. https://doi.org/10.1007/s00382-018-4137-z

Brinkop, S., & Roeckner, E. (1995). Sensitivity of a general circulation model to parameterizations of cloud-turbulence interactions in the atmospheric boundary layer. *Tellus Series A*, *47*(2), 197–220. https://doi.org/10.3402/tellusa.v47i2.11501

Charlton-Perez, A. J., Baldwin, M. P., Birner, T., Black, R. X., Butler, A. H., Calvo, N., et al. (2013). On the lack of stratospheric dynamical variability in low-top versions of the CMIP5 models. *Journal of Geophysical Research: Atmospheres*, *118*, 2494–2505. https://doi.org/10.1002/jgrd.50125

Charron, M., & Manzini, E. (2002). Gravity waves from fronts: Parameterization and middle atmosphere response in a general circulation model. *Journal of the Atmospheric Sciences*, *59*, 923–941. https://doi.org/10.1175/1520-0469(2002)059<0923:GWFFPA>2.0.CO;2

Coddington, O., Lean, J. L., Pilewskie, P., Snow, M., & Lindholm, D. (2016). A solar irradiance climate data record. *Bulletin of the American Meteorological Society*, *97*(7), 1265–1282. https://doi.org/10.1175/BAMS-D-14-00265.1

Crueger, T., Giorgetta, M. A., Brokopf, R., Esch, M., Fiedler, S., Hohenegger, C., et al. (2018). ICON-A, the atmosphere component of the ICON Earth system model. II: Model evaluation. *Journal of Advances in Modeling Earth Systems*, *10*. https://doi.org/10.1029/2017MS001233

Dee, D. P., Uppala, S. M., Simmons, A. J., Berrisford, P., Poli, P., Kobayashi, S., et al. (2011). The ERA-Interim reanalysis: Configuration and performance of the data assimilation system. *Quarterly Journal of the Royal Meteorological Society*, *137*(656), 553–597. https://doi.org/10.1002/qj.828

Dipankar, A., Stevens, B., Heinze, R., Moseley, C., Zängl, G., Giorgetta, M., & Brdar, S. (2015). Large eddy simulation using the general circulation model ICON. *Journal of Advances in Modeling Earth Systems*, *7*, 963–986. https://doi.org/10.1002/2015MS000431

Dubal, M., Wood, N., & Staniforth, A. (2004). Analysis of parallel versus sequential splittings for time-stepping physical parameterizations. *Monthly Weather Review*, *132*(1), 121–132. https://doi.org/10.1175/1520-0493(2004)131%3C0121:AOPVSS%3E2.0.CO;2

Dubal, M., Wood, N., & Staniforth, A. (2005). Mixed parallel–sequential-split schemes for time-stepping multiple physical parameterizations. *Monthly Weather Review*, *133*(4), 989–1002. https://doi.org/10.1175/MWR2893.1

Eyring, V., Bony, S., Meehl, G. A., Senior, C. A., Stevens, B., Stouffer, R. J., & Taylor, K. E. (2016). Overview of the Coupled Model Intercomparison Project Phase 6 (CMIP6) experimental design and organization. *Geoscientific Model Development*, *9*(5), 1937–1958. https://doi.org/10.5194/gmd-9-1937-2016

Eyring, V., Lamarque, J.-F., Hess, P., Arfeuille, F., Bowman, K., Chipperfield, M. P., et al. (2013). Overview of IGAC/SPARC Chemistry-Climate Model Initiative (CCMI) community simulations in support of upcoming ozone and climate assessments. *SPARC Newsletter*, *40*, 48–66.

Fiedler, S., Stevens, B., & Mauritsen, T. (2017). On the sensitivity of anthropogenic aerosol forcing to model-internal variability and parameterizing a Twomey effect. *Journal of Advances in Modeling Earth Systems*, *9*, 1325–1341. https://doi.org/10.1002/2017MS000932

Fritts, D. C., & Nastrom, G. D. (1992). Sources of mesoscale variability of gravity waves. II. Frontal, convective and jet stream excitation. *Journal of the Atmospheric Sciences*, *49*, 111–127. https://doi.org/10.1175/1520-0469(1992)049%3C0111:SOMVOG%3E2.0.CO;2

Gassmann, A., & Herzog, H. J. (2008). Towards a consistent numerical compressible non-hydrostatic model using generalized Hamiltonian tools. *Quarterly Journal of the Royal Meteorological Society*, *134*(635), 1597–1613. https://doi.org/10.1002/qj.297

Gates, W. L. (1992). AMIP: The Atmospheric Model Intercomparison Project. *Bulletin of the American Meteorological Society*, *73*, 1962–1970. https://doi.org/10.1175/1520-0477(1992)073<1962:ATAMIP>2.0.CO;2

Geller, M. A., Alexander, M. J., Love, P. T., Bacmeister, J., Ern, M., Hertzog, A., et al. (2013). A comparison between gravity wave momentum fluxes in observations and climate models. *Journal of Climate*, *26*(17), 6383–6405. https://doi.org/10.1175/JCLI-D-12-00545.1

Giorgetta, M. A., Jungclaus, J., Reick, C. H., Legutke, S., Bader, J., Böttinger, M., et al. (2013). Climate and carbon cycle changes from 1850 to 2100 in MPI-ESM simulations for the coupled model intercomparison project phase 5. *Journal of Advances in Modeling Earth Systems*, *5*(3), 572–597. https://doi.org/10.1002/jame.20038

Giorgetta, M. A., Manzini, E., Roeckner, E., Esch, M., & Bengtsson, L. (2006). Climatology and forcing of the quasi-biennial oscillation in the MAECHAM5 model. *Journal of Climate*, *19*(16), 3882–3901. https://doi.org/10.1175/JCLI3830.1

Giorgetta, M. A., Roeckner, E., Mauritsen, T., Bader, J., Crueger, T., Esch, M., et al. (2013). The atmospheric general circulation model ECHAM6—Model description. Berichte zur Erdsystemforschung/Max-Planck-Institut für. *Meteorologie*, *135*. http://handle.net/11858/00-001M-0000-0013-FCA5-3

GLOBE Task Team (Hastings, David A., Paula K. Dunbar, Gerald M. Elphingstone, Mark Bootz, Hiroshi Murakami, Hiroshi Maruyama, Hiroshi Masaharu, Peter Holland, John Payne, Nevin A. Bryant, Thomas L. Logan, J.-P. Muller, Gunter Schreier, & John S. MacDonald), eds. (1999). *The Global Land One-kilometer Base Elevation (GLOBE) Digital Elevation Model, Version 1.0*. National Oceanic and Atmospheric Administration, National Geophysical Data Center, 325 Broadway, Boulder, Colorado 80305–3328, U.S.A. Digital data base on the World Wide Web (URL: http://www.ngdc.noaa.gov/mgg/topo/globe.html) and CD-ROMs.

Hagemann, S. (2002). An improved land surface parameter dataset for global and regional climate models, Report/Max-Planck-Institut für. *Meteorologie*, *336*. https://doi.org/10.17617/2.2344576

Hagemann, S., & Stacke, T. (2015). Impact of the soil hydrology scheme on simulated soil moisture memory. *Climate Dynamics*, *44*(7-8), 1731–1750. https://doi.org/10.1007/s00382-014-2221-6

Heinze, R., Dipankar, A., Henken, C. C., Moseley, C., Sourdeval, O., Tromel, S., et al. (2017). Large-eddy simulations over Germany using ICON: A comprehensive evaluation. *Quarterly Journal of the Royal Meteorological Society*, *143*, 69–100. https://doi.org/10.1002/qj.2947

Hines, C. O. (1997). Doppler-spread parameterization of gravity wave momentum deposition in the middle atmosphere: Part 1. Basic formulation. *Journal of Atmospheric and Solar-Terrestrial Physics*, *59*(4), 371–386. https://doi.org/10.1016/S1364-6826(96)00079-X

Hurrell, J. W., Hack, J. J., Shea, D., Caron, J. M., & Rosinski, J. (2008). A new sea surface temperature and sea ice boundary dataset for the Community Atmosphere Model. *Journal of Climate*, *21*(19), 5145–5153. https://doi.org/10.1175/2008JCLI2292.1

Iacono, M. J., Delamere, J. S., Mlawer, E. J., Shephard, M. W., Clough, S. A., & Collins, W. D. (2008). Radiative forcing by long-lived greenhouse gases: Calculations with the AER radiative transfer models. *Journal of Geophysical Research*, *113*, D13103. https://doi.org/10.1029/2008JD009944

Johnson, G. C., Lyman, J. M., & Loeb, N. G. (2016). Improving estimates of Earth's energy imbalance. *Nature Climate Change*, *6*(7), 639–640. https://doi.org/10.1038/nclimate3043

Kato, S., Loeb, N. G., Rose, F. G., Doelling, D. R., Rutan, D. A., Caldwell, T. E., et al. (2013). Surface irradiances consistent with CERES-derived top-of-atmosphere shortwave and longwave irradiances. *Journal of Climate*, *26*(9), 2719–2740. https://doi.org/10.1175/JCLI-D-12-00436.1

Kays, W. M. (1994). Turbulent Prandtl number. Where are we? *ASME Transactions Journal of Heat Transfer*, *116*(2), 284–295. https://doi.org/10.1115/1.2911398

Kinne, S., O'Donnel, D., Stier, P., Kloster, S., Zhang, K., Schmidt, H., et al. (2013). MAC-v1: A new global aerosol climatology for climate studies. *Journal of Advances in Modeling Earth Systems*, *5*, 704–740. https://doi.org/10.1002/jame.20035

Klocke, D., Brueck, M., Hohenegger, C., & Stevens, B. (2017). Rediscovery of the doldrums in storm-resolving simulations over the tropical Atlantic. *Nature Geoscience*, *10*(12), 891–896. https://doi.org/10.1038/s41561-017-0005-4

Krismer, T., & Giorgetta, M. A. (2014). Wave forcing of the quasi-biennial oscillation in the Max Planck Institute Earth System Model. *Journal of the Atmospheric Sciences*, *71*(6), 1985–2006. https://doi.org/10.1175/JAS-D-13-0310.1

Leuenberger, D., Koller, M., Fuhrer, O., & Schär, C. (2010). A generalization of the SLEVE vertical coordinate. *Monthly Weather Review*, *138*(9), 3683–3689. https://doi.org/10.1175/2010MWR3307.1

Loeb, N. G., Wielicki, B. A., Doelling, D. R., Smith, G. L., Keyes, D. F., Kato, S., et al. (2009). Toward optimal closure of the Earth's top-of-atmosphere radiation budget. *Journal of Climate*, *22*(3), 748–766. https://doi.org/10.1175/2008JCLI2637.1

Lohmann, U., & Roeckner, E. (1996). Design and performance of a new cloud microphysics scheme developed for the ECHAM general circulation model. *Climate Dynamics*, *12*(8), 557–572. https://doi.org/10.1007/BF00207939

Lott, F. (1999). Alleviation of stationary biases in a GCM through a mountain drag parame- terization scheme and a simple representation of mountain lift forces. *Monthly Weather Review*, *127*(5), 788–801. https://doi.org/10.1175/1520-0493(1999)127%3C0788:AOSBIA%3E2.0.CO;2

Lott, F., & Miller, M. J. (1997). A new-subgrid-scale orographic drag parameterization: Its formulation and testing. *Quarterly Journal of the Royal Meteorological Society*, *123*(537), 101–127. https://doi.org/10.1002/qj.49712353704

Manzini, E., & McFarlane, N. A. (1998). The effect of varying the source spectrum of a gravity wave parameterization in a middle atmosphere general circulation model. *Journal of Geophysical Research*, *103*(D24), 31,523–31,539. https://doi.org/10.1029/98JD02274

Matthes, K., Funke, B., Andersson, M. E., Barnard, L., Beer, J., Charbonneau, P., et al. (2017). Solar forcing for CMIP6 (v3.2). *Geoscientific Model Development*, *10*(6), 2247–2302. https://doi.org/10.5194/gmd-10-2247-2017

Mauritsen, T., Stevens, B., Roeckner, E., Crueger, T., Esch, M., Giorgetta, M., et al. (2012). Tuning the climate of a global model. *Journal of Advances in Modeling Earth Systems*, *4*, M00A01. https://doi.org/10.1029/2012MS000154

Mauritsen, T., & Svensson, G. (2007). Observations of stably stratified shear-driven atmospheric turbulence at low and high Richardson numbers. *Journal of the Atmospheric Sciences*, *64*(2), 645–655. https://doi.org/10.1175/JAS3856.1

Mauritsen, T., Svensson, G., Zilitinkevich, S. S., Esau, I., Enger, L., & Grisogono, B. (2007). A total turbulent energy closure model for neutrally and stably stratified atmospheric boundary layers. *Journal of the Atmospheric Sciences*, *64*(11), 4113–4126. https://doi.org/10.1175/2007JAS2294.1

Meinshausen, M., Vogel, E., Nauels, A., Lorbacher, K., Meinshausen, N., Etheridge, D. M., et al. (2017). Historical greenhouse gas concentrations for climate modelling (CMIP6). *Geoscientific Model Development*, *10*(5), 2057–2116. https://doi.org/10.5194/gmd-10-2057-2017

Mlawer, E. J., Taubman, S. J., Brown, P. D., Iacono, M. J., & Clough, S. A. (1997). Radiative transfer for inhomogeneous atmospheres: RRTM, a validated correlated-k model for the longwave. *Journal of Geophysical Research*, *102*(D14), 16,663–16,682. https://doi.org/10.1029/97JD00237

Möbis, B., & Stevens, B. (2012). Factors controlling the position of the Intertropical Convergence Zone on an aquaplanet. *Journal of Advances in Modeling Earth Systems*, *4*, M00A04. https://doi.org/10.1029/2012MS000199

Nordeng, T. E. (1994). Extended versions of the convective parameterization scheme at ECMWF and their impact on the mean transient activity of the model in the tropics, ECMWF Tech. Memo., 206, 41 pp.

Pincus, R., Barker, H. W., & Morcrette, J.-J. (2003). A fast, flexible, approximate technique for computing radiative transfer in inhomogeneous cloud fields. *Journal of Geophysical Research*, *108*(D13), 4376. https://doi.org/10.1029/2002JD003322

Pincus, R., & Stevens, B. (2009). Monte Carlo spectral integration: A consistent approximation for radiative transfer in large eddy simulations. *Journal of Advances in Modeling Earth Systems*, *1*, 1. https://doi.org/10.3894/james.2009.1.1

Pincus, R., & Stevens, B. (2013). Paths to accuracy for radiation parameterizations in atmospheric models. *Journal of Advances in Modeling Earth Systems*, *5*, 225–233. https://doi.org/10.1002/jame.20027

Pithan, F., Angevine, W., & Mauritsen, T. (2015). Improving a global model from the boundary layer: Total turbulent energy and the neutral limit Prandtl number. *Journal of Advances in Modeling Earth Systems*, *7*, 791–805. https://doi.org/10.1002/2014MS000382

Quaas, J. (2012). Evaluating the critical relative humidity as a measure of subgrid-scale variability of humidity in general circulation model cloud cover parameterizations using satellite data. *Journal of Geophysical Research*, *117*, D09208. https://doi.org/10.1029/2012JD017495

Raddatz, T. J., Reick, C. H., Knorr, W., Kattge, J., Roeckner, E., Schnur, R., et al. (2007). Will the tropical land biosphere dominate the climate-carbon cycle feedback during the twenty-first century? *Climate Dynamics*, *29*(6), 565–574. https://doi.org/10.1007/s00382-007-0247-8

Räisänen, P., & Barker, H. W. (2004). Evaluation and optimization of sampling errors for the Monte Carlo independent column approximation. *Quarterly Journal of the Royal Meteorological Society*, *130*(601), 2069–2085. https://doi.org/10.1256/qj.03.215

Reichler, T., & Kim, J. (2008). How well do coupled models simulate today's climate? *Bulletin of the American Meteorological Society*, *89*(3), 303–312. https://doi.org/10.1175/BAMS-89-3-303

Schirber, S., Manzini, E., & Alexander, M. J. (2014). A convection-based gravity wave parameterization in a general circulation model: Implementation and improvements on the QBO. *Journal of Advances in Modeling Earth Systems*, *6*, 264–279. https://doi.org/10.1002/2013MS000286

Siebesma, A. P., & Cuijpers, J. W. (1995). Evaluation of parametric assumptions for shallow cumulus convection. *Journal of the Atmospheric Sciences*, *52*, 650–666. https://doi.org/10.1175/1520-0469(1995)052<0650:EOPAFS>2.0.CO;2

Silvers, L. G., Stevens, B., Mauritsen, T., & Giorgetta, M. (2016). Radiative convective equilibrium as a framework for studying the interaction between convection and its large-scale environment. *Journal of Advances in Modeling Earth Systems*, *8*, 1330–1344. https://doi.org/10.1002/2016MS000629

Smiatek, G., Rockel, B., & Schättler, U. (2008). Time invariant data preprocessor for the climate version of the COSMO model (COSMO-CLM). *Meteorologische Zeitschrift*, *17*(4), 395–405. https://doi.org/10.1127/0941-2948/2008/0302

Stenchikov, G. L., Kirchner, I., Robock, A., Graf, H.-F., Antuña, J. C., Grainger, R. G., et al. (1998). Radiative forcing from the 1991 Mount Pinatubo volcanic eruption. *Journal of Geophysical Research*, *103*(D12), 13,837–13,857. https://doi.org/10.1029/98JD00693

Stevens, B., Fiedler, S., Kinne, S., Peters, K., Rast, S., Müsse, J., & Mauritsen, T. (2017). MACv2-SP: A parameterization of anthropogenic aerosol optical properties and an associated Twomey effect for use in CMIP6. *Geoscientific Model Development*, *10*(1), 433–452. https://doi.org/10.5194/gmd-10-433-2017

Stevens, B., Giorgetta, M., Esch, M., Mauritsen, T., Crueger, T., Rast, S., et al. (2013). Atmospheric component of the MPI-M Earth System Model: ECHAM6. *Journal of Advances in Modeling Earth Systems*, *5*, 146–172. https://doi.org/10.1002/jame.20015

Sundqvist, H., Berge, E., & Kristjánsson, J. E. (1989). Condensation and cloud parame- terization studies with a mesoscale numerical weather prediction model. *Monthly Weather Review*, *117*(8), 1641–1657. https://doi.org/10.1175/1520-0493(1989)117%3C1641:CACPSW%3E2.0.CO;2

Taylor, K., Williamson, D., & Zwiers, F. (2000). The sea surface temperature and sea- ice concentration boundary conditions for AMIP II simulations, PCMDI Rep, 60 (28).

Tiedtke, M. (1989). A comprehensive mass flux scheme for cumulus parameterization in large-scale models. *Monthly Weather Review*, *117*, 1779–1800. https://doi.org/10.1175/1520-0493(1989)117<1779:ACMFSF>2.0.CO;2

Tomita, H., Tsugawa, M., Satoh, M., & Goto, K. (2001). Shallow water model on a modified icosahedral grid by using spring dynamics. *Journal of Computational Physics*, *174*(2), 579–613. https://doi.org/10.1006/jcph.2001.6897

Wan, H., Giorgetta, M. A., Zängl, G., Restelli, M., Majewski, D., Bonaventura, L., et al. (2013). The ICON-1.2 hydrostatic atmospheric dynamical core on triangular grids—Part 1: Formulation and performance of the baseline version. *Geoscientific Model Development*, *6*(3), 735–763. https://doi.org/10.5194/gmd-6-735-2013

Watterson, I. G., Dix, M. R., & Colman, R. A. (1999). A comparison of present and doubled CO2 climates and feedbacks simulated by three general circulation models. *Journal of Geophysical Research*, *104*(D2), 1943–1956. https://doi.org/10.1029/1998JD200049

Williamson, D. L. (2002). Time-split versus process-split coupling of parameterizations and dynamical core. *Monthly Weather Review*, *130*(8), 2024–2041. https://doi.org/10.1175/1520-0493(2002)130%3C2024:TSVPSC%3E2.0.CO;2

Yeo, K. L., Krivova, N. A., Solanki, S. K., & Glassmeier, K. H. (2014). Reconstruction of total and spectral solar irradiance from 1974 to 2013 based on KPVT, SoHO/MDI and SDO/HMI observations. *Astronomy & Astrophysics*, *570*, A85. https://doi.org/10.1051/0004-6361/201423628

Zängl, G., Reinert, D., Ripodas, P., & Baldauf, M. (2015). The ICON (ICOsahedral Non-hydrostatic) modelling framework of DWD and MPI-M: Description of the non-hydrostatic dynamical core. *Quarterly Journal of the Royal Meteorological Society*, *141*(687), 563–579. https://doi.org/10.1002/qj.2378

Zhang, G. J., Wu, X., & Mitovski, T. (2016). Estimation of convective entrainment properties from cloud-resolving model simulation during TWP-ICE. *Climate Dynamics*, *47*(7-8), 2177–2192. https://doi.org/10.1007/s00382-015-2957-7